University Library

MINERVA ACCESS

A gateway to Melbourne's research publications

Minerva Access is the Institutional Repository of The University of Melbourne

Author/s:
Buquicchio, FA;Fonseca, R;Yan, PK;Wang, F;Evrard, M;Obers, A;Gutierrez, JC;Raposo, CJ;Belk, JA;Daniel, B;Zareie, P;Yost, KE;Qi, Y;Yin, Y;Nico, KF;Tierney, FM;Howitt, MR;Lareau, CA;Satpathy, AT;Mackay, LK

Title:
Distinct epigenomic landscapes underlie tissue-specific memory T cell differentiation

Date:
2024-09-10

Citation:
Buquicchio, F. A., Fonseca, R., Yan, P. K., Wang, F., Evrard, M., Obers, A., Gutierrez, J. C., Raposo, C. J., Belk, J. A., Daniel, B., Zareie, P., Yost, K. E., Qi, Y., Yin, Y., Nico, K. F., Tierney, F. M., Howitt, M. R., Lareau, C. A., Satpathy, A. T. & Mackay, L. K. (2024). Distinct epigenomic landscapes underlie tissue-specific memory T cell differentiation. Immunity, 57 (9), pp.2202-2215.e6. https://doi.org/10.1016/j.immuni.2024.06.014.

Persistent Link:
https://hdl.handle.net/11343/350482

Resource

Immunity

Distinct epigenomic landscapes underlie tissue-specific memory T cell differentiation

Graphical abstract

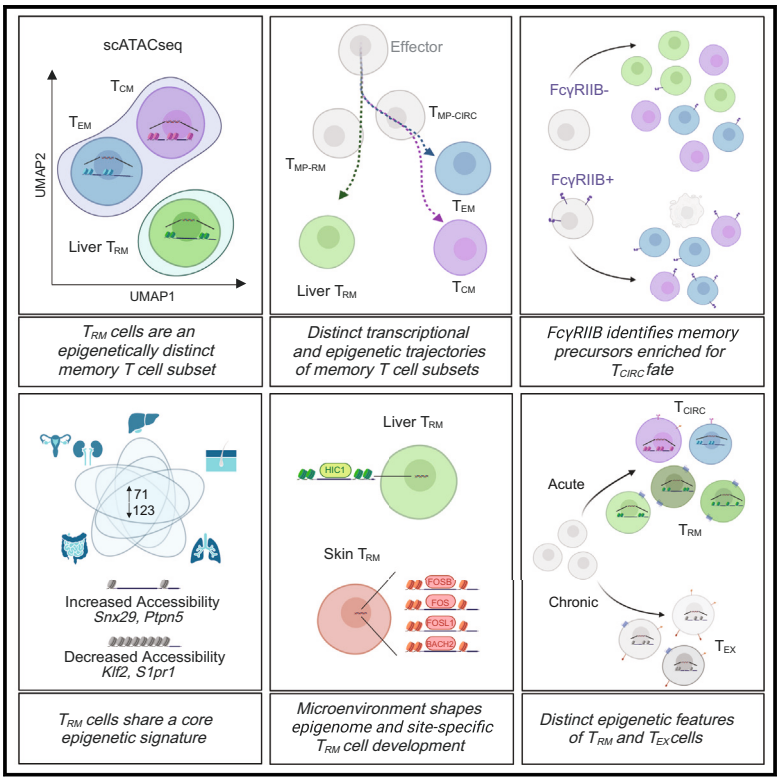

Highlights

- Memory T cell subsets develop along distinct epigenetic trajectories
- T_{RM} cells exhibit a distinct chromatin landscape from that of T_{CIRC} cell subsets
- Epigenetic analyses reveal novel organ-specific regulators of T_{RM} cell development
- T_{RM} and T_{EX} are epigenetically distinct but exhibit *cis*-regulatory element overlap

Authors

Frank A. Buquicchio, Raissa Fonseca, Patrick K. Yan, ..., Caleb A. Lareau, Ansuman T. Satpathy, Laura K. Mackay

Correspondence

satpathy@stanford.edu (A.T.S.), lkmackay@unimelb.edu.au (L.K.M.)

In brief

Epigenomic features steering CD8$^+$ T cell heterogeneity across tissues has not yet been extensively explored. By profiling chromatin accessibility changes and gene expression in T cells derived from multiple organs, Buquicchio et al. reveal the epigenetic state of memory CD8$^+$ T cells and identify subset and organ-specific regulators involved in T cell differentiation.

Buquicchio et al., 2024, Immunity *57*, 2202–2215
September 10, 2024 © 2024 Elsevier Inc. All rights reserved, including those for text and data mining, AI training, and similar technologies.
https://doi.org/10.1016/j.immuni.2024.06.014

CellPress

CellPress

Immunity

Resource

Distinct epigenomic landscapes underlie tissue-specific memory T cell differentiation

Frank A. Buquicchio,[1,2,6,7] Raissa Fonseca,[3,7] Patrick K. Yan,[1,2] Fangyi Wang,[1,2] Maximilien Evrard,[3] Andreas Obers,[3] Jacob C. Gutierrez,[1,2] Colin J. Raposo,[1,2] Julia A. Belk,[1,4] Bence Daniel,[1] Pirooz Zareie,[3] Kathryn E. Yost,[1] Yanyan Qi,[1] Yajie Yin,[1,2] Katherine F. Nico,[1,2] Flora M. Tierney,[1,2] Michael R. Howitt,[1,2] Caleb A. Lareau,[1,2,5,6] Ansuman T. Satpathy,[1,2,5,6,8,*] and Laura K. Mackay[3,8,9,*]

[1]Department of Pathology, Stanford University, Stanford, CA 94305, USA
[2]Program in Immunology, Stanford University, Stanford, CA 94304, USA
[3]Department of Microbiology and Immunology, The University of Melbourne at The Peter Doherty Institute for Infection and Immunity, Melbourne, VIC 3000, Australia
[4]Department of Computer Science, Stanford University, Stanford, CA 94305, USA
[5]Parker Institute for Cancer Immunotherapy, Stanford University, Stanford, CA 94129, USA
[6]Gladstone-UCSF Institute of Genomic Immunology, San Francisco, CA 94158, USA
[7]These authors contributed equally
[8]These authors contributed equally
[9]Lead contact
*Correspondence: satpathy@stanford.edu (A.T.S.), lkmackay@unimelb.edu.au (L.K.M.)
https://doi.org/10.1016/j.immuni.2024.06.014

SUMMARY

The memory CD8$^+$ T cell pool contains phenotypically and transcriptionally heterogeneous subsets with specialized functions and recirculation patterns. Here, we examined the epigenetic landscape of CD8$^+$ T cells isolated from seven non-lymphoid organs across four distinct infection models, alongside their circulating T cell counterparts. Using single-cell transposase-accessible chromatin sequencing (scATAC-seq), we found that tissue-resident memory T (T_{RM}) cells and circulating memory T (T_{CIRC}) cells develop along distinct epigenetic trajectories. We identified organ-specific transcriptional regulators of T_{RM} cell development, including FOSB, FOS, FOSL1, and BACH2, and defined an epigenetic signature common to T_{RM} cells across organs. Finally, we found that although terminal T_{EX} cells share accessible regulatory elements with T_{RM} cells, they are defined by T_{EX}-specific epigenetic features absent from T_{RM} cells. Together, this comprehensive data resource shows that T_{RM} cell development is accompanied by dynamic transcriptome alterations and chromatin accessibility changes that direct tissue-adapted and functionally distinct T cell states.

INTRODUCTION

CD8$^+$ T cells are key mediators of protective immunity against infectious diseases and tumors. Following antigen encounters, recently activated T cells infiltrate sites of infection where they mediate pathogen control and generate long-lasting heterogeneous memory T cell populations. Although some memory T cells circulate throughout the blood and lymphatics (including central memory [T_{CM}] and effector memory [T_{EM}] T cells or T_{CIRC} collectively), others are permanently stationed in peripheral organs. These non-migratory tissue-resident memory T (T_{RM}) cells have been identified in all organs across different species.[1,2]

Variations in distinct tissue microenvironments, cytokine exposure, antigen persistence, and T cell receptor (TCR) signal strength poise T cells at different stages and shape the effector response, culminating in the development of heterogeneous CD8$^+$ T cell subsets.[3–9] Some of these populations of memory CD8$^+$ T cells display distinct stem-like properties and functional capabilities and offer varied degrees of immune protection.[10–15] In certain contexts, such as chronic infections or tumors, continuous antigen recognition leads to the development of exhausted T (T_{EX}) cells that display reduced functional ability and increased expression of inhibitory receptors, compared with memory T cell populations.[16–20] The introduction and expansion of high-throughput sequencing technologies have enhanced our definitions of the transcriptional and epigenetic changes associated with T cell differentiation and heterogeneity.[21–23]

Dynamic genome-wide analysis of DNA methylation and chromatin accessibility during T_{CIRC} cell development has demonstrated the complex determination of effector and memory T cell fates in mice and humans.[24–26] Epigenomic profiling of single cells has demonstrated changes in *cis*- and *trans*-regulatory elements associated with regulation of gene expression in individual subsets, allowing for the reconstruction of trajectories associated with cellular differentiation.[27,28] Although it is known that heterogeneous T_{CIRC}, T_{RM}, and T_{EX} cells exist and rely on distinct transcriptional circuitries, when their differentiation

 © 2024 Elsevier Inc.
All rights are reserved, including those for text and data mining, AI training, and similar technologies.

trajectories diverge and the epigenomic changes steering their ontogeny are not clear.

Here, we examined transcriptional and chromatin accessibility changes in $CD8^+$ T cells isolated from distinct anatomical sites following acute and chronic infection in mice. Over the course of acute lymphocytic choriomeningitis virus (LCMV) infection, we observed an early epigenetic bifurcation in T_{RM} and T_{CIRC} precursors in the liver, indicative of disparate developmental trajectories. This early diversion in effector cell fate was marked by differential *Fcgr2b* accessibility and Fc gamma Receptor IIB (FcγRIIB) expression, allowing the selection of memory precursors with enhanced capacity to generate either liver T_{RM} or T_{CIRC} populations. Although T_{RM} cells were epigenetically distinct from T_{CIRC} cells, analyses of T_{RM} cells isolated from different organs revealed transcription factors (TFs) that regulated T_{RM} cell formation in an organ-specific manner, including FOSB, FOS, FOSL1, and BACH2. Furthermore, dissection of T_{RM} cells within each organ revealed intra-tissue heterogeneity that was associated with conserved networks of TFs, including KLF and HIC factors. Finally, we showed that among T_{EX} cell subsets, terminal T_{EX} ($T_{EX\text{-}TERM}$) cells uniquely shared accessibility in *cis*-regulatory elements that were contained within the core T_{RM} cell epigenetic signature. Together, our data demonstrate that distinct epigenetic landscapes define T_{RM} cell differentiation and form the basis for organ-specific phenotypic and transcriptional differences. Additionally, we provide public genome browsers for interrogating the chromatin accessibility profiles of $CD8^+$ effector and memory T cells, as well as T_{RM} and T_{EX} cells, to support future investigations.

RESULTS

T_{RM} cells are an epigenetically distinct subset of memory T cells

To investigate the epigenetic landscape of $CD8^+$ T cell populations, we first utilized a model of acute viral infection in combination with TCR transgenic $CD8^+$ T cells. To this end, we transferred congenically marked ($CD45.1^+$) naive $CD8^+$ P14 T cells specific for the LCMV glycoprotein-derived epitope 33–41 (GP33) into mice infected with LCMV Armstrong (Arm) to generate memory $CD8^+$ T cells across organs. At 30 days post-infection (d p.i.), P14 T cells were isolated from the liver and spleen, alongside P14 T cells from naive mice, and cells were subjected to single-cell transposase-accessible chromatin sequencing (scATAC-seq)[27] (Figures 1A and S1A). Fifteen thousand seven hundred forty single cells passed quality control filters of at least 1,000 unique fragments per cell and a transcription start site (TSS) enrichment score greater than or equal to 5 (Figure S1B).

To analyze scATAC-seq profiles, we utilized ArchR[29] (1) for dimensionality reduction using latent sematic indexing (LSI), uniform manifold approximation and projection (UMAP) embedding, and cell clustering[30,31]; (2) to identify changes in accessibility of individual *cis*-regulatory regions (“peaks”) in the genome; (3) to calculate deviation in accessibility of TF motifs; (4) to validate changes in accessibility observed in genomic tracks; (5) to predict “marker peaks” or changes in accessibility of genes that are specific to a given cluster; (6) to calculate a single accessibility metric for each gene (“gene score”) based on locus and distal regulatory element accessibility weighted by distance; and (7) to perform pseudo-time differentiation trajectory analysis to model epigenomic changes that occur over the course of a projected differentiation trajectory (Figure S1C).

Dimensionality reduction and visualization by UMAP revealed four distinct clusters that aligned with sort-purified naive, T_{EM}, T_{CM}, and T_{RM} populations (Figures 1B and 1C). Although we found little distinction between the chromatin state of the liver and splenic T_{EM} and T_{CM} cells, liver T_{RM} cells comprised a discrete cluster (Figures 1B and 1C). Upon comparison of T cell clusters, we observed that the number of chromatin accessible peaks exclusive to T_{RM} cells (2,424 increased, 4,007 decreased; $\log_2$ fold change [FC] > 1, $-\log_{10}$ false discovery rate [FDR] > 10) was similar in magnitude to the number of T_{EM} (2,491, 7,552) and T_{CM} (2,213, 1,276) cell-exclusive peaks, whereas T_{EM} and T_{CM} cells shared a proportionally higher number of peaks (2,120, 2,416) (Figure 1D), indicating that each T cell population exhibits distinct epigenetic profiles.

To link differentially accessible peaks to genes, we examined gene-level accessibility changes across the gene body and within linked distal sites using gene scores.[29,32] Direct comparison of gene scores between T_{RM} and T_{EM} or T_{CM} cell clusters revealed differential accessibility in peaks corresponding to genes with decreased expression in T_{RM} cells compared with T_{CIRC} cells, such as *Klf2*, *Ccr7*, *Sell*, *S1pr5*, *Zeb2*, and *Cx3cr1* (Figure 1E). This analysis also revealed differential accessibility in genes with no known role in liver T_{RM} cell formation, such as *Fcgr2b* and *Hic1*, as well as increased accessibility in adhesion-related genes, such as *Chn2*, *Cdh1*, *Itga9*, and *Gpr55*, a G-protein-coupled receptor known to regulate intraepithelial lymphocyte (IEL) migration[33] (Figures 1E and 1F). To confirm if the observed gene score changes were also observed at the transcriptional level, we compared genes with differential accessibility with previously published transcriptional profiles from T_{EM}, T_{CM}, and liver T_{RM} cells.[4] Accordingly, T_{RM} cells displayed increased *Gpr55* and *Hic1* gene expression and decreased *Fcgr2b* expression when compared with T_{EM} and T_{CM} cells (Figure S1D). Diminished gene scores for *Ccr7* and *Sell* were also observed in T_{EM} relative to T_{CM} cell clusters (*Sell*; $\log_2$FC = −0.327, $-\log_{10}$FDR = 2.45. *Ccr7*; $\log_2$FC = −0.820, $-\log_{10}$FDR = 24.20), as well as increased accessibility at the *S1pr5* and *Zeb2* loci (Figures S1E and S1F), indicating that chromatin accessibility identifies archetypal features of T cell identity.

Given that decreased expression of *Klf2* and *S1pr1* is a prerequisite for T_{RM} cell development,[6] we verified that chromatin accessibility was reduced across *Klf2* and *S1pr1* gene loci, alongside decreased KLF2 motif accessibility in T_{RM} cells when compared with T_{EM} and T_{CM} cells (Figures 1G and 1H). By contrast, although the chromatin accessibility of *Hic1* was specifically increased in the liver T_{RM} population (Figure 1F), HIC1 motif accessibility was significantly reduced in T_{RM} cells relative to other subsets (Figure 1H). This is consistent with the known interaction of HIC1 with polycomb repressive complex 2 (PRC2), which plays a role in chromatin compaction and transcriptional repression.[34] Nonetheless, CRISPR-Cas9-mediated *Hic1* deletion in $CD8^+$ T cells showed that liver T_{RM} cells require this TF for development (Figures S1G and S1H), similar to T_{RM} cells in the small intestine (SI).[35] To investigate the changes in chromatin accessibility induced by the loss of HIC1, we performed ATAC-seq on sg*Hic1* and sgCtrl P14 T cells isolated

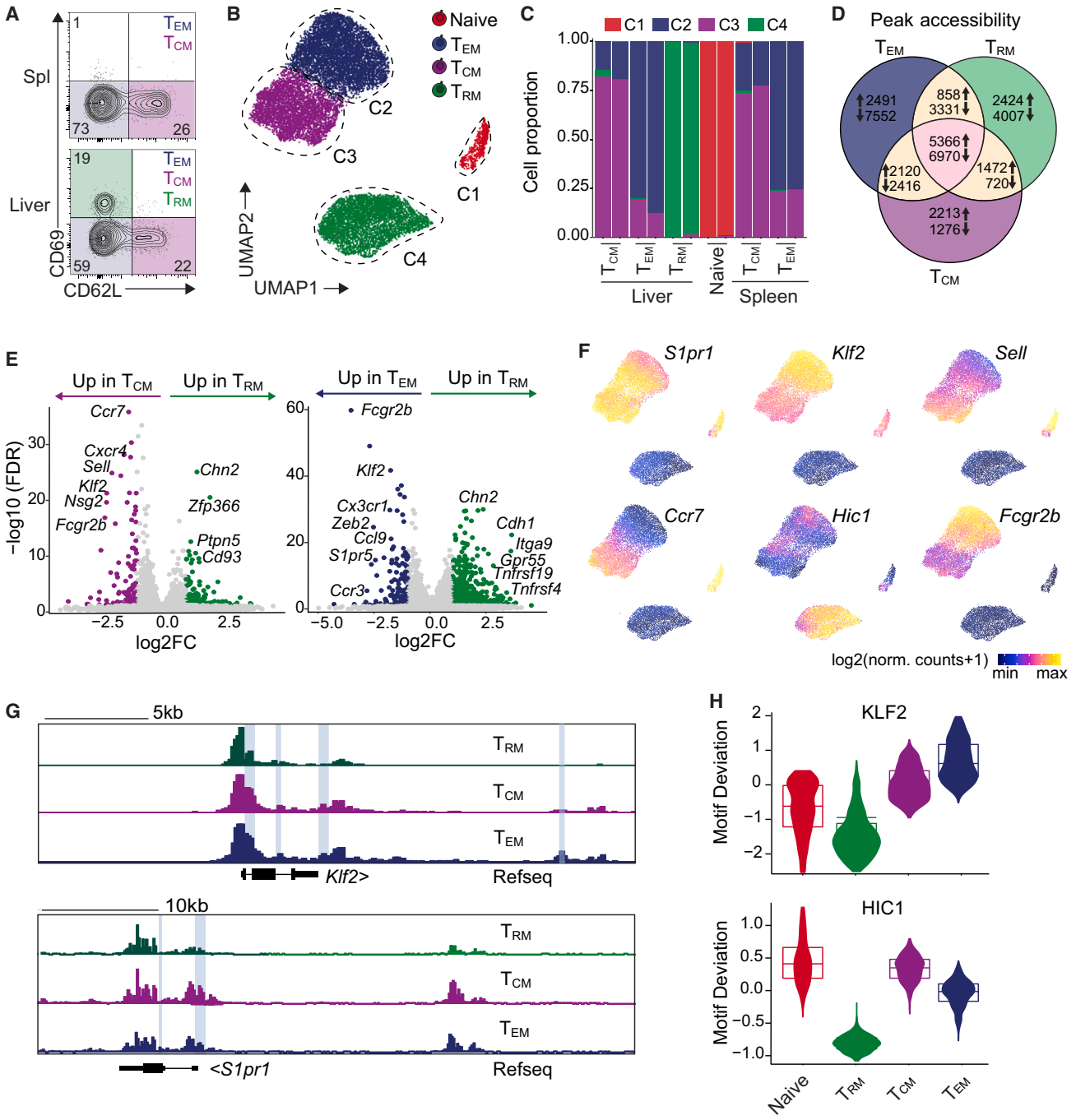

Figure 1. T_{RM} cells display a unique epigenetic landscape amidst memory T cell subsets

(A–H) Congenically marked CD45.1$^+$ naive CD8$^+$ P14 T cells were transferred into C57BL/6 mice that were subsequently infected with LCMV Arm. P14 T cell subsets (classified as T_{CM} [CD62L$^+$CD69$^-$], T_{EM} [CD62L$^-$CD69$^-$], and T_{RM} [CD62L$^-$CD69$^+$]) cells were isolated from the spleen and liver 30 d p.i., alongside P14 T cells (CD44$^-$CD62L$^+$) from naive mice. scATAC-seq was performed. (A) Sorting schematic of P14 T cell populations from the spleen (spl) and liver. (B) UMAP projection of scATAC-seq data. (C) Cluster composition by sample identity based on sorted T cell subsets. (D) Venn diagram of differential peaks in identified clusters compared with naive cells ($log_2FC > 1$, FDR < 0.05). (E) Gene score volcano plots identifying genes with differential accessibility ($log_2FC > 1$, FDR < 0.05) between T_{RM} and T_{EM} or T_{CM} cell clusters; notable genes annotated manually. (F) UMAP depicting gene scores across clusters. (G) *Klf2* and *S1pr1* genome tracks (height normalized) and (H) KLF2 and HIC1 motif deviation in naive and memory T cell clusters. Data are pooled from (A–H) two independent experiments with *n* = 5 mice each. Boxplots show the median and interquartile ranges.

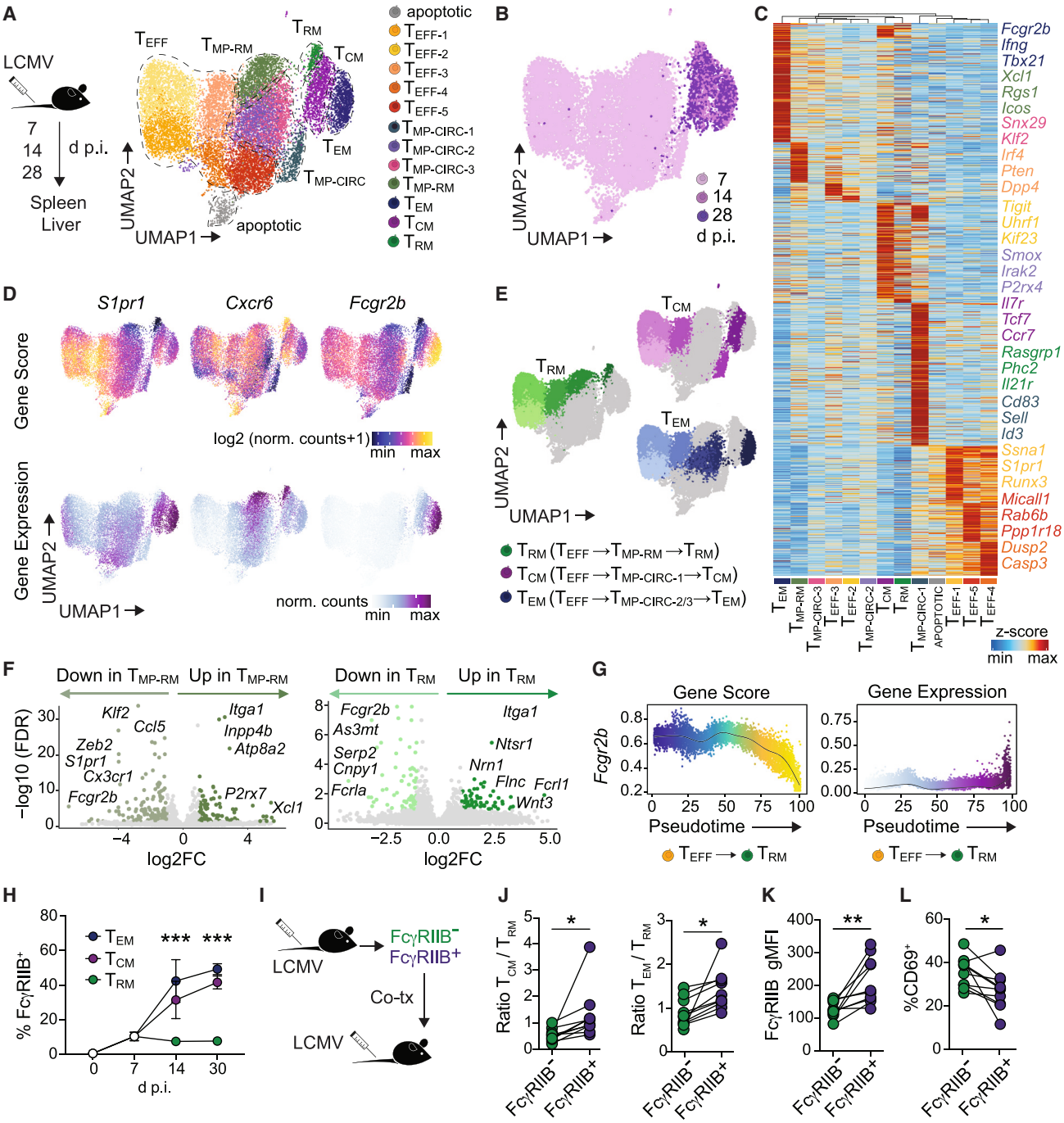

Figure 2. Distinct epigenetic trajectories define T_{CIRC} and T_{RM} cell development

(A–G) C57BL/6 mice were infected with LCMV Arm, and H-2D(b)-GP33 tetramer$^+$ cells were isolated from the liver and spleen at 7, 14, and 28 d p.i. Paired scRNA/scATAC-seq was performed. (A) Experimental schematics and UMAP projection of scRNA/scATAC-seq profiles with clusters highlighted. (B) UMAP depicting d p.i. (C) Marker peak heatmap identifying *cis*-regulatory elements active in individual clusters; peaks associated with notable genes are annotated and colored by cluster. (D) UMAP depicting *S1pr1*, *Cxcr6*, and *Fcgr2b* gene scores (top) and gene expression (bottom). (E) Predicted differentiation trajectories of memory T cell clusters. (F) Genes with differential accessibility in $T_{MP\text{-}RM}$ (relative to $T_{MP\text{-}CIRC\text{-}1\text{-}3}$) and T_{RM} (relative to T_{CIRC}) cells. (G) *Fcgr2b* gene score and gene expression over pseudotime for the T_{RM} cell trajectory.

(H) Congenically marked naive P14 T cells were transferred into LCMV Arm infected mice. Livers were harvested 7, 14, and 30 d p.i. Flow cytometry analysis of FcγRIIB expression at indicated time points.

(legend continued on next page)

from the liver of LCMV Arm infected mice 30 d p.i. We found 137 and 175 peaks with increased and decreased accessibility, respectively (Figure S1I), which included genes involved in the regulation of cell cycle and apoptosis.[36,37] Altogether, these data demonstrate that T_{RM}, T_{EM}, and T_{CM} cells are epigenetically distinct memory T cell subsets, with scATAC-seq effectively highlighting unique chromatin features in each T cell population.

Memory T cell subsets display distinct epigenetic trajectories

Several studies have suggested that T_{RM} and T_{CIRC} cells may arise from distinct progenitor populations.[38–40] Given that chromatin accessibility precedes gene transcription, we utilized single-cell multiome sequencing (scATAC + scRNA sequencing [RNA-seq])[41,42] to investigate epigenetic and transcriptional changes that occur during $CD8^+$ T cell differentiation after LCMV Arm infection. We isolated GP33 $tetramer^+$ $CD8^+$ T cells from the liver and spleen at 7, 14, and 28 d p.i. Cluster analysis showed that GP33 $tetramer^+$ T cells isolated at 7 d p.i. comprised 10 clusters, whereas cells isolated at 14 and 28 d p.i. were comparatively less diverse, consisting of 3 clusters (Figures 2A, 2B, and S2A) that were enriched for T_{CIRC} or T_{RM} cell gene signatures (Figure S2B). Within effector cells (T_{EFF}) isolated at 7 d p.i., we found clusters expressing genes associated with proliferation and cytotoxicity (*Mki67*, *Top2a*, *Gzmb*, and *Pfn1*; data not shown) ($T_{EFF\text{-}1\text{-}5}$), as well as clusters that showed an enrichment for T_{CIRC} or T_{RM} cell gene signatures that we termed memory T cell precursors (T_{MP} [$T_{MP\text{-}CIRC1\text{-}3}$, $T_{MP\text{-}RM}$]) (Figure S2B). $T_{MP\text{-}CIRC\text{-}1}$ and $T_{MP\text{-}CIRC\text{-}2\text{-}3}$ cells displayed increased accessibility and gene expression of T_{CM}-related (e.g., *Sell*, *Il7r*) and T_{EM}-defining genes (e.g., *Tbx21*, *Ifng*, and *Fcgr2b*), respectively (Figures 2C and S2C). $T_{MP\text{-}RM}$ cells showed enrichment in the T_{RM} cell gene signature, as well as increased *Cd69* and reduced *S1pr1* accessibility and expression, hallmark features of T_{RM} cells (Figures 2D and S2D). Additionally, $T_{MP\text{-}RM}$ cells displayed the highest enrichment in the liver T_{RM} cell epigenetic signature (as defined in Figure 1), whereas $T_{MP\text{-}CIRC\text{-}1\text{-}3}$ cells exhibited a chromatin state reflective of T_{CIRC} cells (Figures S2B–S2E).

We next utilized pseudotime trajectory analysis to infer the developmental relationships of $CD8^+$ T cells as they differentiate into discrete subsets. Given that the adoptive transfer of T_{EFF} cells can give rise to both T_{RM} and T_{CIRC} cell subsets following infection,[15] we designated the T_{EFF} cell clusters as a starting point and used either $T_{MP\text{-}CIRC}$ or $T_{MP\text{-}RM}$ cell clusters as the branching point (Figure 2E). We observed changes associated with T_{RM} cell development (e.g., increased *Cxcr6* and decreased *Sell*, *S1pr1*, and *Cx3cr1* gene scores) along the T_{EFF} to T_{RM} cell trajectory (Figures S2F and S2G), reflective of protein expression changes observed by flow cytometry (Figure S2H). To identify molecules shared between putative T_{RM} cell precursors and bona fide T_{RM} cells, we examined genes with differential accessibility between $T_{MP\text{-}RM}$ and $T_{MP\text{-}CIRC\text{-}1\text{-}3}$ or T_{RM} and T_{CIRC} cell clusters (Figure 2F). The FcγRIIB locus displayed reduced accessibility in $T_{MP\text{-}RM}$ and T_{RM} cells, compared with $T_{MP\text{-}CIRC\text{-}1\text{-}3}$ and T_{CIRC} cells (Figure 2F). This change in *Fcgr2b* accessibility was reflected by FcγRIIB protein expression in T cells at 30 d p.i. (Figures 2G, 2H, and S2I).

To investigate whether FcγRIIB marks T cells with a differential capacity to form T_{CIRC} or T_{RM} cells, we sort-purified congenically marked FcγRIIB$^-$ and FcγRIIB$^+$ P14 T cells from the spleen 7 d p.i. and adoptively transferred these cells into infection-matched recipient mice (Figure 2I). Although the progeny of FcγRIIB$^+$ cells preferentially gave rise to T_{EM} and T_{CM} cells, cells lacking FcγRIIB displayed an increased propensity to form T_{RM} cells in the liver (Figures 2J–2L). In line with this, the genetic deletion of *Fcgr2b* in P14 T cells resulted in the reduction of T_{EM} and T_{CM} cells without impacting liver T_{RM} cell development (Figures S2J–S2L). Consistent with the known role of FcγRIIB in apoptosis,[43] we found increased active caspase-3/-7 in liver T_{RM} cells in FcγRIIB$^+$ cells compared with FcγRIIB$^-$ cells (Figure S2M). Although further validation is required to define bona fide lineage commitment, these results indicate that effector T cells navigate distinct memory T cell trajectories and highlight the differential accessibility and expression of genes that may identify cells poised for distinct T cell fates.

T_{RM} cells share a common epigenetic signature across different organs

Transcriptional and protein profiling of T_{RM} cells across different organs, infection models, and species has demonstrated that these cells exhibit conserved modifications associated with tissue retention across models, such as reduced KLF2 and increased CD69 expression.[4,5,11,39] To assess if T_{RM} cells also share a common epigenetic profile across organs, we utilized congenically marked naive TCR transgenic cells specific for epitopes within LCMV Arm (P14), Herpes simplex virus (HSV [gBT-I]), or ovalbumin (*Listeria monocytogenes*-OVA or influenza X31-OVA [OT-I]) to compare the chromatin accessibility profiles of T_{RM} cells derived from the liver, SI-IEL, salivary glands (SGs), female reproductive tract (FRT), kidney, lung, and skin vs. their T_{CIRC} cell counterparts (Figures 3A and S3A). Isolated cells were subjected to scATAC-seq, filtered, analyzed, and visualized by UMAP (Figure 3A). Although T_{RM} cells isolated from SI-IEL, lung, skin, and liver clustered separately, we found that those derived from the SGs, FRT, and kidney were predominantly present in one cluster (Figures 3A and S3B), suggesting that T cells adopt a common epigenetic program associated with tissue residence in these organs.

To identify features involved in driving T_{RM} cell epigenetic heterogeneity, we sought to determine if organ-specific T_{RM} populations exhibited conserved accessibility in *cis*-regulatory elements, relative to their respective T_{CIRC} populations. From 82,067 differentially accessible peaks in T_{RM} relative to T_{CIRC} cell clusters (Table S1), we found 71 peaks with increased accessibility and 123 peaks with decreased accessibility that were common to

(I–L) Distinct congenically marked naive P14 T cells were transferred into LCMV Arm infected mice. FcγRIIB$^-$ and FcγRIIB$^+$ cells were isolated from the spleen at 7 d p.i. and co-transferred into infection-matched recipients. Transferred cells were isolated from the spleen and liver 30 d p.i. (I) Experimental schematics. (J) Proportion of T_{CM} or T_{EM} and T_{RM} cells, (K) FcγRIIB, and (L) CD69 expression in transferred FcγRIIB$^-$ and FcγRIIB$^+$ T cells. Data are representative from (A–G) 5 mice per time point, (H) 2 independent experiments with n =10 mice each, or pooled from (I–L) 2 independent experiments with n = 5 mice each. In (H) symbols represent mean ± SEM or (J–L) individual mice. * $p \leq 0.05$, ** $p \leq 0.01$, *** $p \leq 0.001$, ns $p > 0.05$, (H) one-way ANOVA with Bonferroni post-test, (J–L) two-tailed Student's t test.

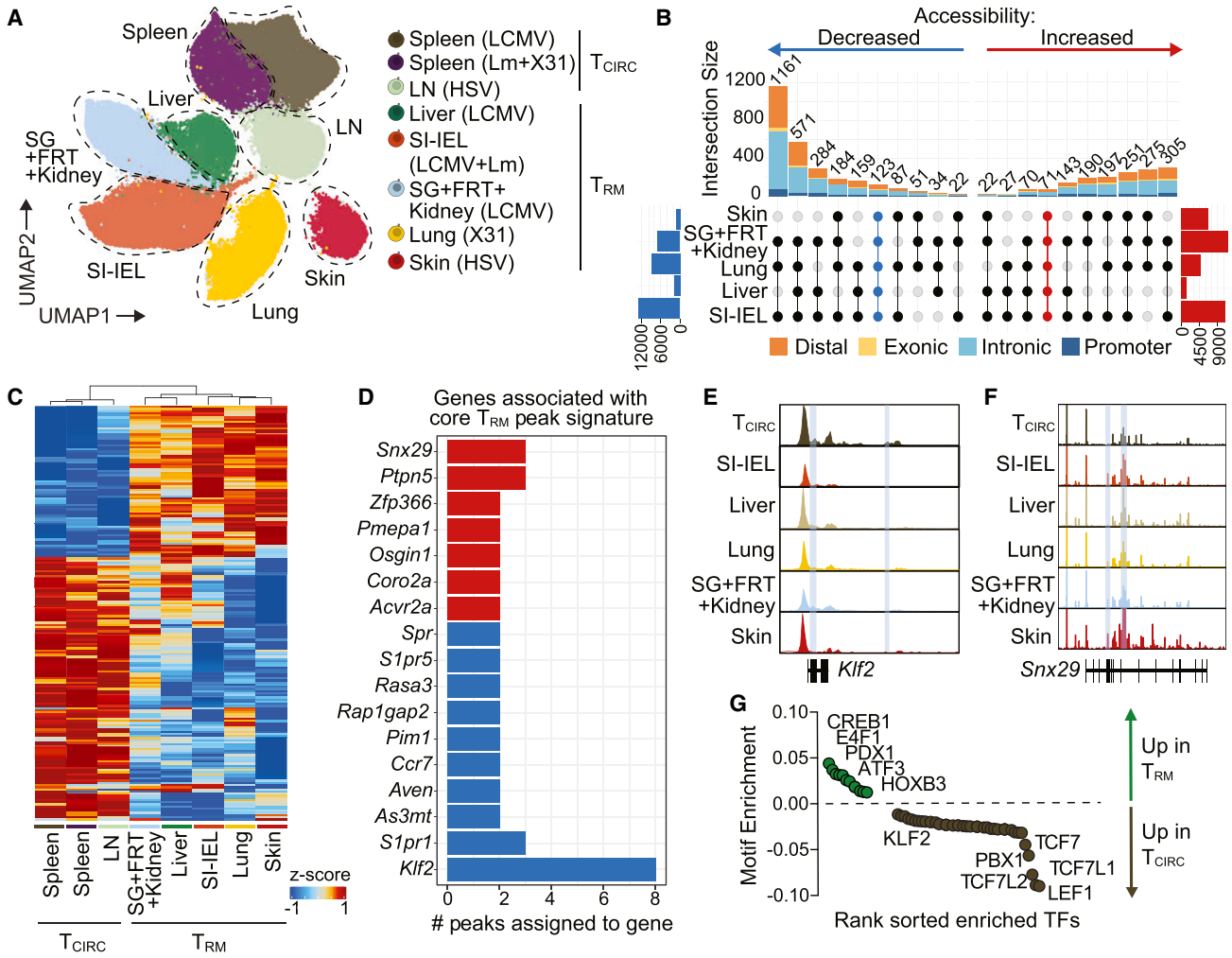

Figure 3. T_{RM} cells share a common epigenetic signature across tissues

(A–G) Congenically marked naive TCR transgenic cells were transferred into mice infected with either LCMV Arm (P14), HSV (gBT-I), *Listeria monocytogenes*-OVA [Lm], or influenza X31-OVA [X31] (OT-I) (n = 77,966 cells). The indicated organs were harvested 30 d p.i., and scATAC-seq was performed. (A) UMAP projection of scATAC-seq data. (B) UpSet plot of T_{RM} peaks across organs. (C) Marker peak heatmap of shared peaks in T_{RM} vs. T_{CIRC} cell clusters and (D) genes with more than 2 peaks with increased (red) or decreased (blue) accessibility. (E and F) Genome track of (E) *Klf2* and (F) *Snx29* in cluster aggregated scATAC-seq data (height normalized). (G) Motif enrichment analysis of T_{RM} vs. T_{CIRC} cell clusters. Data are pooled from (A–G) 2 independent experiments with n = 5–20 mice.

T_{RM} cells in all organs analyzed ($\log_2$FC > 0.5, $-\log_{10}$FDR ≥ 1) (Figures 3B and 3C; Table S2). Mapping peaks with differential accessibility to genes revealed that *Klf2* and *S1pr1* exhibited the most frequent losses in *cis*-regulatory element accessibility, whereas *Snx29* and *Ptpn5* exhibited the most frequent gains in *cis*-regulatory element accessibility (Figures 3D–3F). To further understand gene-level accessibility changes unique to T_{RM} cells, we identified significant gene score changes relative to T_{CIRC} cells and observed 52 and 37 genes with decreased and increased accessibility, respectively, including *Ptpn5* and *Litaf* (Figures S3C and S3D). Next, we asked whether *cis*-regulatory elements shared enrichment for TF motifs in T_{RM} cells across all organs. We found a broad enrichment in motifs belonging to CREB1, E4F1, PDX1, and ATF3 in T_{RM} cells while T_{CIRC} cells were enriched in motifs for KLF2, LEF1, and TCF7, as expected from previous studies[44] (Figures 3G and S3E; Table S3).

We next sought to compare genes from this common epigenetic signature with those from previously published T_{RM} cell "core" signatures (from bulk[4,39] and scRNA-seq datasets[35]). Forty-four genes were uniquely identified by scATAC-seq, including *Acvr2a*, *Ptpn5*, and *Snx29* (Figure S3F). Genes shared across datasets included *Xcl1*, *Cish*, *Litaf*, and *Qpct* (Figure S3F), although such commonalities were relatively few and were likely attributable to the diverse range of organs, infection models, and time points collectively studied. Given this, we restricted our comparison to T_{RM} cells from a single organ.[35,38] Indeed, we observed 3,867 overlapping genes between different SI-IEL ATAC-seq datasets, 60 overlapping genes between different scRNA-seq datasets, and 27 genes that were differentially accessible or differentially expressed in SI-IEL across all datasets analyzed (Figure S3G). Together, by defining a conserved T_{RM} cell epigenetic signature and identifying genes (including

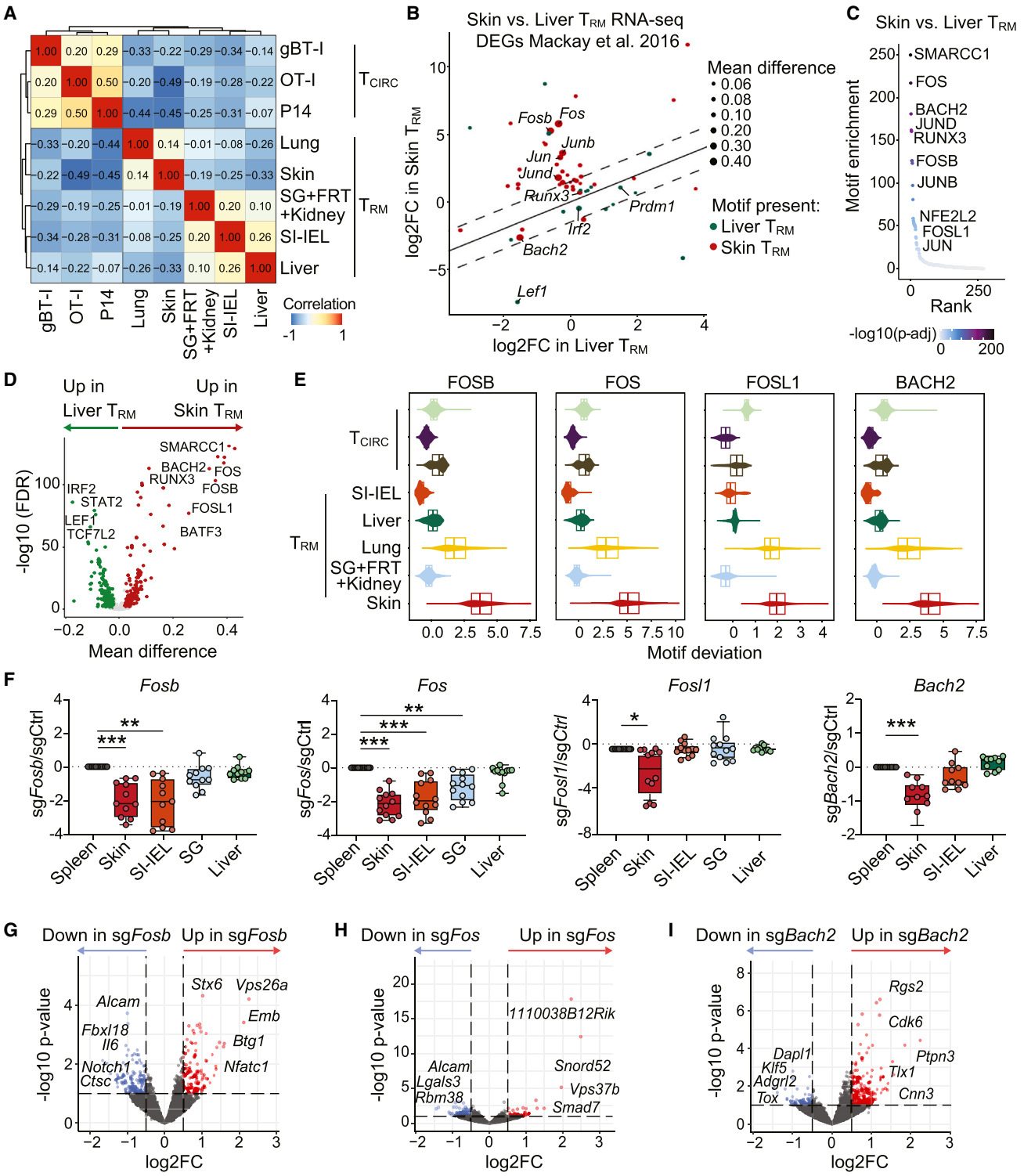

Figure 4. Tissue-specific epigenetic signatures depict transcriptional regulators of T_{RM} cell development

(A–E) As in Figures 3A–3G. (A) Correlation plot of marker peaks from memory T cells ($log_2FC > 1$, FDR < 0.05). (B) TFs with significant motif deviations between skin and liver T_{RM} cell clusters were selected and paired with DEGs between skin and liver T_{RM} (relative to T_{CM}) cells from GEO: GSE70813. (C) Motif enrichment analysis in skin T_{RM} cell-exclusive peaks and (D) volcano plot depicting skin and liver T_{RM} cell-exclusive motifs. (E) FOSB, FOS, FOSL1, and BACH2 motif deviations in indicated populations.

(legend continued on next page)

Snx29, *Ptpn5*) and *trans*-regulatory factors (CREB1 and PDX1) not previously implicated in T_{RM} cell fate, these data demonstrate the utility of using epigenetic analyses to uncover new regulatory elements associated with T_{RM} cell development.

Local microenvironment shapes T_{RM} cell epigenome and promotes site-specific differentiation

Despite sharing core transcriptional and core epigenetic signatures, T_{RM} cells exhibit vast organ-specific phenotypic heterogeneity regulated by distinct molecular cues.[45] To define epigenetic features associated with tissue residency across different organs, we selected marker peaks ($log_2FC \geq 1.5$, $-log_{10}FDR \geq 10$) that defined each T_{RM} population (Figure S4A) and performed pathway enrichment analyses. Among enriched pathways, participation of transforming growth factor-β (TGF-β) signaling was observed in skin and SI IEL T_{RM} cells, whereas liver T_{RM} cells were enriched in interferon (IFN) signaling (Figure S4B) in line with previous findings.[3,46–48] To assess which T_{RM} populations exhibited the most divergent chromatin accessibility across organs, we calculated Pearson correlation using the defined marker peaks. We found that among T_{RM} populations, those in the liver and skin exhibited the strongest negative correlation (Figure 4A). To identify putative regulators of these distinct chromatin landscapes, we integrated motif accessibility data from liver and skin T_{RM} cells with previously published RNA-seq data[4] to identify expressed TFs. We found 53 TFs that were differentially active and/or differentially expressed in skin T_{RM} cells relative to liver T_{RM} cells, including *Fosb*, *Fos*, and *Jun* (change in accessibility and expression) and *Bach2* (change in motif accessibility only) (Figures 4B–4D and S4C), with skin T_{RM} cells displaying the highest motif accessibility for FOSB, FOS, FOSL1, and BACH2 across all clusters (Figure 4E).

Given these results, we hypothesized that the FOS family members and BACH2 would affect T_{RM} cell differentiation in the skin, but not in the liver. To test this, we used CRISPR-Cas9 to ablate either *Fosb*, *Fos*, *Fosl1*, or *Bach2* in P14 T cells, which were co-transferred with sgCtrl cells into mice infected with LCMV Arm and treated with 2,4-dinitrofluorobenzene (DNFB) on the flank to induce skin T_{RM} cells.[49] To observe location-specific defects in memory T cell formation, we compared the number of P14 T cells in the skin, SI-IEL, SG, and liver with those in the spleen. Indeed, the deletion of *Fosb*, *Fos*, *Fosl1*, and *Bach2* dramatically impaired skin T_{RM} cell formation while leaving T_{RM} cells in the liver unaffected (Figure 4F). Similarly, in the absence of *Fosb*, *Fos*, and *Fosl1*, skin T_{RM} cell development was impaired after HSV infection (Figure S4D), demonstrating the participation of the FOS TF family in skin T_{RM} cell formation.

To investigate how disruption in these TFs impacted the chromatin state of T cells, we performed bulk ATAC-seq on single guide RNA (sgRNA)-targeted cells isolated from the spleen and found that genetic ablation of *Fosb* led to a decrease in 115 peaks, including genes involved in the interleukin (IL)-12 signaling pathway (Figures 4G and S4E). Deletion of *Fos* led to a decrease in 53 peaks, affecting pathways related to focal adhesion kinases and SMAD2/3 signaling (Figures 4H and S4F), consistent with the role of FOS in SMAD3-mediated transcription of TGF-β-induced genes.[50] Although mostly unique peaks were affected by the absence of FOS and FOSB, a reduction in accessibility of genes related to IL-23 signaling was observed in the absence of both TFs (Figures S4E and S4F). Furthermore, deletion of *Bach2* led to a decrease in 21 peaks, including peaks located in *Adgrl2* and *Tox* and affected pathways involved in TCR and nuclear factor κB (NF-κB) (Figures 4I and S4G). Altogether, our data show that although T_{RM} cells show a core residency signature, epigenetic analyses identify regulators that are essential for the establishment of tissue residency in different tissues.

Analysis of intra-tissue T_{RM} cell heterogeneity indicates a conserved program across tissues

Intra-tissue $CD8^+$ T_{RM} cell heterogeneity has been explored using single-cell transcriptional analyses in the skin and SI.[12,51] To evaluate if T_{RM} cells residing in each organ also display epigenetic heterogeneity, we segmented each T_{RM} cell cluster and assessed the chromatin state of subclusters within organs (Figure 5A). Given recent findings that BLIMP-1 denotes either effector or memory-biased T_{RM} populations in the SI,[12] we sought to evaluate if such differences might be observed at the epigenetic level. For this, we used chromVAR to assess motif variation based on CisBP database predictions and evaluated the gene score associated with *Prdm1*. Indeed, distinct subclusters of T_{RM} cells with differential accessibility in BLIMP-1 motifs and gene scores were observed across organs (Figure 5B). To next investigate if intra-organ T_{RM} cell heterogeneity was driven by common TFs, we used CisBP and JASPAR databases to select TFs with differential motif accessibility between T_{RM} subclusters in each organ and then restricted analyses to the most relevant motifs by selecting TFs with significant gene expression in T_{CIRC} and T_{RM} cells[4] (Figures S5A–S5D). Although CisBP revealed 30 TF motifs shared between one subcluster from each organ—group A (skin T_{RM-2}, SG+FRT+kidney T_{RM-1}, lung T_{RM-1}, liver T_{RM-2}, and SI-IEL T_{RM-2}), JASPAR identified eight motifs shared across group A clusters (Figure 5C). Similarly, group B subclusters (skin T_{RM-1}, SG+FRT+kidney T_{RM-2}, lung T_{RM-2}, liver T_{RM-1}, and SI-IEL T_{RM-1}) exhibited 13 and 2 TFs with consistent motif accessibility across organs using CisBP and JASPAR, respectively (Figure 5C). While both databases were enriched in motifs for ASCL2, HIC1, PTF1A, and TCF in group A subclusters, group B was enriched in motifs for ARNTL and KLF

(F) Distinct congenically marked naive P14 T cells were activated *in vitro*, and ablation of *Fosb*, *Fos*, *Fosl1*, and *Bach2* was performed using CRISPR-Cas9. Cells were transferred into LCMV Arm infected recipients that were treated with DNFB. P14 T cells were isolated from the spleen, skin, SI-IEL, SG, and liver 30 d p.i. log_2FC of edited P14 T cells in the indicated tissues (relative to sgCtrl) normalized to the spleen.

(G–I) Distinct congenically marked naive P14 T cells were activated *in vitro*, and ablation of *Fosb*, *Fos*, and *Bach2* was performed using CRISPR-Cas9. Cells were transferred into LCMV Arm infected recipients. P14 T cells were isolated from the spleen 30 d p.i. ATAC-seq was performed. Differential peak volcano plot between (G) sg*Fosb*, (H) sg*Fos*, or (I) sg*Bach2* (relative to sgCtrl) cells. Data are pooled from (A–E) 2 independent experiments with $n = 5–20$ pooled mice and (F–I) 2 independent experiments with $n = 5–6$ mice each. In (F) symbols represent individual mice. Boxplots show the median, interquartile range, and minimum/maximum whiskers. * $p \leq 0.05$, ** $p \leq 0.01$, *** $p \leq 0.001$, ns $p > 0.05$, one-way ANOVA with Bonferroni post-test.

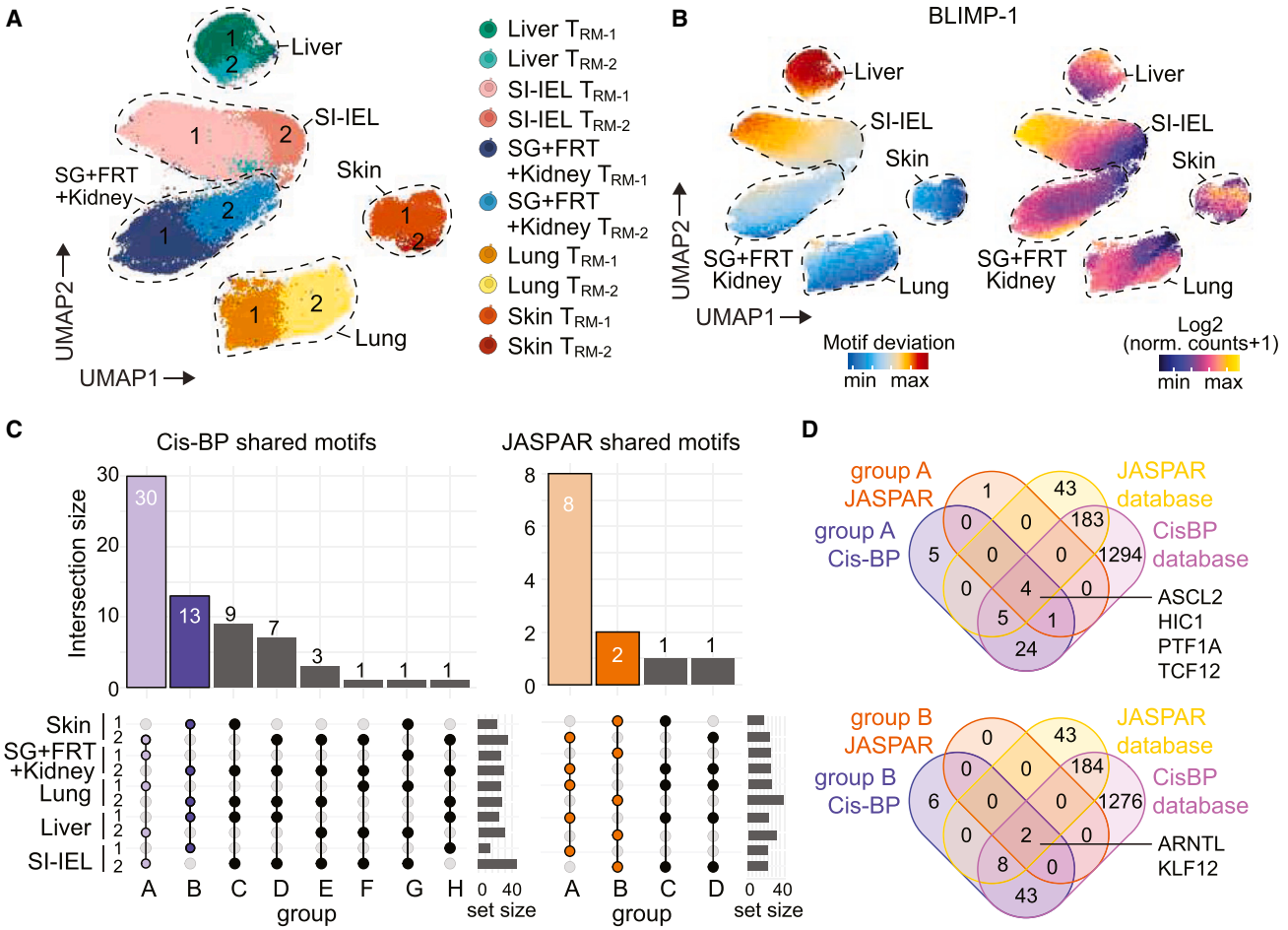

Figure 5. Distinct molecular regulators define T_{RM} cell intra-tissue epigenetic heterogeneity across organs

(A–D) Congenically marked naive TCR transgenic cells were transferred into mice infected with either LCMV Arm (P14), HSV (gBT-I), *Listeria monocytogenes*-OVA [Lm], or influenza X31-OVA [X31] (OT-I) (n = 77,966 cells). The indicated organs were harvested 30 d p.i., and scATAC-seq was performed on isolated transgenic T cell populations. (A) UMAP projection of T_{RM} cell subclusters in the indicated organs. (B) UMAP projection depicting BLIMP-1 motif and gene score. (C) UpSet plots identifying shared motifs in T_{RM} cell subclusters across organs forming groups A (skin T_{RM-2}, SG+FRT+kidney T_{RM-1}, lung T_{RM-1}, liver T_{RM-2}, and SI-IEL T_{RM-2}) and B (skin T_{RM-1}, SG+FRT+kidney T_{RM-2}, lung T_{RM-2}, liver T_{RM-1}, and SI-IEL T_{RM-1}) using CisBP (left) or JASPAR (right) databases. (D) Venn diagram depicting TF motifs observed in groups A (top) and B (bottom) using CisBP and JASPAR databases.

(Figure 5D). Together, these data suggest an overlap in TFs associated with the intra-tissue T_{RM} cell heterogeneity across tissues.

Shared and unique epigenetic features define exhausted and tissue-resident T cells

T_{EX} cells share transcriptional and functional phenotypes with T_{RM} cells[3,12] with common TFs such as BHLHE40 and BAF complexes required for the development of both subsets.[52–54] To this point, it remains unclear whether the transcriptional overlap between these T cell populations is indicative of a shared epigenetic state. First, we compared RNA-seq data from skin, SI-IEL, or liver T_{RM} cells following HSV or LCMV Arm infection[4] with T_{EX} cells generated in response to LCMV clone-13 (c13, chronic infection), which induces a characteristic T_{EX} cell phenotype.[55] We observed shared transcriptional features between T_{RM} and T_{EX} cells, including in genes related to the core T_{RM} cell gene signature (Figures 6A and 6B). Similarly, protein expression of molecules associated with T_{RM} and T_{EX} cells showed that similar to LCMV c13 generated T_{EX} cells, skin T_{RM} cells generated by HSV infection expressed high levels of PD1 and TIM3, whereas liver T_{RM} cells exhibited comparatively reduced expression of these molecules, reinforcing variation in organ-specific T_{RM} populations (Figures S6A–S6C).

There are multiple epigenetic states of T cell exhaustion, and T_{EX} populations exhibit distinct functionality and differentiation potential.[56–60] To explore the existence of epigenetic similarities between T_{EX} cell subsets and T_{RM} cells, we compared our T_{RM} cell scATAC-seq dataset with previously published data characterizing the epigenome of T_{EX} cells.[60] We integrated scATAC-seq data from GP33 tetramer$^+$ CD8$^+$ T cells isolated from LCMV c13 infected mice at 8 and 21 d p.i.[60] with scATAC-seq data of liver, skin, SG, FRT, kidney, lung, and SI-IEL T_{RM} cells (Figures 6C and S6D). T_{EX} cells separated into four distinct clusters, as previously described, which were annotated as 8 d p.i. early effector ($_{Eeff}$) T_{EX} cells and 21 d p.i. progenitor ($_{PROG}$),

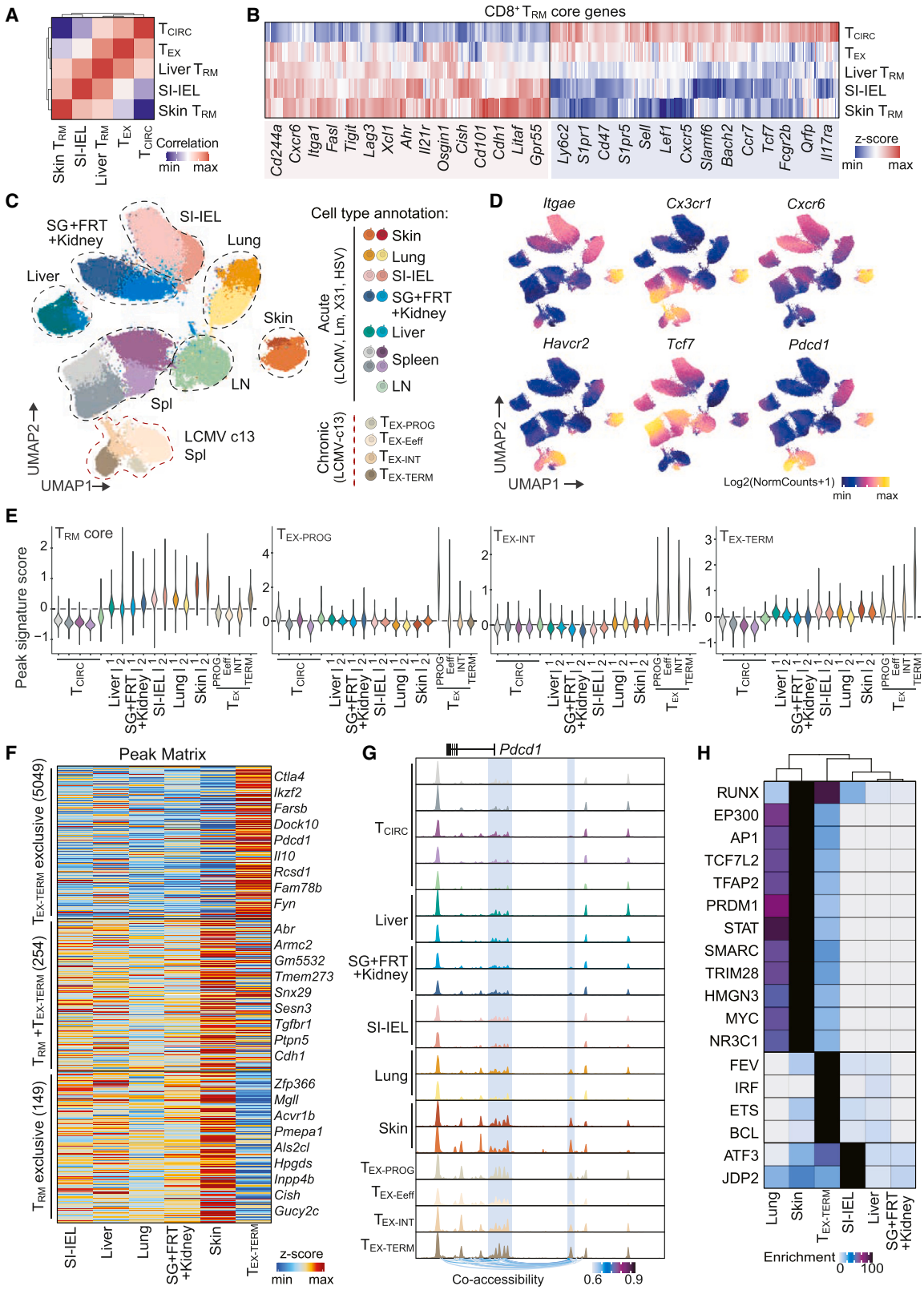

Figure 6. Shared and unique epigenetic features of T_{RM} and T_{EX} cells

(A and B) RNA-seq data from skin, SI-IEL, and liver T_{RM} cells (GEO: GSE70813) were integrated with T_{EX} cells (GEO: GSE84820), and transcriptional analysis was performed. (A) Correlation matrix of DEGs and (B) heatmap of T_{RM} cell core genes expression by the indicated T cell subsets.

(legend continued on next page)

intermediate ($_{INT}$), and terminal ($_{TERM}$) T_{EX} cells[61] using *Havcr2*, *Cx3cr1*, *Pdcd1*, and *Tcf7* gene scores (Figure 6D). Cells originated from chronic infection clustered separately from those isolated during acute infections at all stages of differentiation, highlighting an overall distinct chromatin state for T_{RM} and T_{EX} cells (Figures S6E and S6F).

Next, we sought to compare gene and motif accessibility associated with T cell exhaustion. We found that *Tox* gene scores were reduced in T_{RM} cells when compared with all T_{EX} cell subsets (Figure S6G), supporting low *Tox* expression in T_{RM} cells (Figure S6H). Additionally, similar to expression at the protein level, increased *Tcf7* gene scores were observed in $T_{EX\text{-}PROG}$ cells and T_{CM} cells when compared with T_{RM} or other T_{EX} populations (Figures S6G and S6H), consistent with the increased stemness and differentiation capacity of these populations. Motif deviation for several T_{EX}-associated TFs, such as IRF4 and EOMES, was highest in T_{EX} cell clusters (Figures S6I and S6J). RUNX3, however, exhibited the highest motif deviation in the skin T_{RM} population and $T_{EX\text{-}TERM}$ cells (Figure S6J).

To assess epigenetic features shared between T_{RM} and T_{EX} cells, we compared gene accessibility from each T_{EX} cell subset isolated at 21 d p.i. to marker peaks defined in T_{RM} and T_{CIRC} cell clusters (Table S4). Although we observed an enrichment of shared T_{RM} cell peaks in $T_{EX\text{-}TERM}$ cells (mean deviation = 0.3332, *Z* score = 3.036), $T_{EX\text{-}PROG}$ or $T_{EX\text{-}INT}$ cell clusters were not enriched in peaks that defined T_{RM} cells (Figure 6E). Similarly, liver, SI-IEL, lung, and skin T_{RM} cell clusters were enriched in $T_{EX\text{-}TERM}$ peaks, with no enrichment observed for $T_{EX\text{-}PROG}$ or $T_{EX\text{-}INT}$ peaks in the T_{RM} cell clusters (Figure 6E). Additionally, we observed that SI-IEL T_{RM} cells exhibited the most shared changes in chromatin accessibility with $T_{EX\text{-}TERM}$ cells (1,605 decreased and 1,019 increased peaks, Figure S6K).

To explore the accessibility of *cis*-regulatory elements driving this similarity, we assessed the overlap between peaks present in all T_{RM} populations and the $T_{EX\text{-}TERM}$ cell cluster (Figure 6F). Among 254 shared peaks, we identified increased accessibility in multiple peaks located in *Snx29*, *Ptpn5*, and *Cdh1* in these subsets (Figures 6F and S6L). Two of the peaks shared between skin T_{RM} cells and T_{EX} cells were nearest to the *Pdcd1* gene; one peak ~23kb from the TSS of *Pdcd1* is a known T_{EX} cell enhancer that mediates sustained PD1 expression, previously thought to be specific to T_{EX} cells[56,62] (Figure 6G). Although the similarities between the $T_{EX\text{-}TERM}$ and T_{RM} cell clusters were notable, we observed a greater number of *cis*-regulatory elements unique to $T_{EX\text{-}TERM}$ cells (Figure 6G). Among the 5,049 $T_{EX\text{-}TERM}$ cell peaks that were not observed in any T_{RM} populations studied here, 54 were linked to *Tox*, 11 to *Nfatc1*, and 10 to *Batf*, consistent with the roles of those TFs in mediating T cell exhaustion[63–67] (Figures 6F and S6L).

Finally, to identify *trans*-regulatory elements involved in the epigenetic state of T_{RM} and $T_{EX\text{-}TERM}$ cells, we performed motif enrichment analyses on marker peaks that defined each population (Figure 6F). We observed an enrichment of RUNX motifs predominantly in skin T_{RM} and $T_{EX\text{-}TERM}$ cells and that FEV, IRF, ETS, and BCL motifs were largely enriched in $T_{EX\text{-}TERM}$ cells (Figure 6H). Given the dissimilarity in accessibility of *cis*-regulatory elements between early-stage T_{EX} and T_{RM} cells, our results indicate that exhaustion differentiation occurs through a distinct epigenetic mechanism from that steering tissue residency formation. Additionally, although the partial epigenetic similarities between $T_{EX\text{-}TERM}$ and T_{RM} cells underlie the shared transcriptional phenotypes between the cell types, $T_{EX\text{-}TERM}$ cells are defined by a unique set of *cis*-regulatory elements that are largely absent in T_{RM} cells.

DISCUSSION

Here, we used an unbiased single-cell resolution approach to examine the epigenetic and transcriptomic changes that occur during $CD8^+$ memory T cell development. Using trajectory analyses, we modeled peak accessibility, TF motif deviation, and gene expression changes during T cell differentiation over time after viral infections. In line with previous studies indicative of early T cell commitment to the T_{RM} cell lineage,[39,40] our results identified *cis*- and *trans*-regulatory elements that may identify effector cells poised to give rise to distinct T_{RM} or T_{CIRC} cell populations. As such, cells expressing FcγRIIB displayed an increased bias to form T_{CIRC} cells, relative to T_{RM} cells upon transfer. Although additional investigation will be required to identify definitive precursors for each memory T cell population, our data provide additional support for the early fate commitment of T_{RM} cells.

In addition, we demonstrated that T_{RM} cells are an epigenetically distinct T cell subset that share both conserved and unique epigenomic signatures across organs. We identified an epigenetic signature conserved between T_{RM} cells from different organs, consisting of key gene regulatory networks associated with tissue residency and consistent prior RNA-seq analyses demonstrating a common T_{RM} cell transcriptional program.[4,39] Furthermore, we leveraged our chromatin accessibility data to identify potential transcriptional regulators that support tissue-specific T_{RM} cell formation and validated the role of several TFs, including FOSB, FOS, FOSL1, and BACH2, adding to their previously established role in T cell memory, limiting the expression of TCR-driven genes during T cell effector responses.[68,69] Although both enriched motifs and increased expression were observed for the FOS family TFs, BACH2 differential activity could only be detected at the epigenetic level.

Our work also examined whether phenotypic and transcriptional overlap between T_{RM} cells and T_{EX} cells[3,39] reflects a shared epigenetic state. Here, our analyses of chromatin accessibility indicated that the epigenetic changes underlying T cell exhaustion are distinct from those involved in the establishment of T_{RM} cells. Although $T_{EX\text{-}TERM}$ cells display shared accessibility in a number of peaks with T_{RM} cells, early T_{EX} subsets are not enriched in peaks typical of T_{RM} cells. The accessibility of T_{RM}

(C–H) As in Figures 3A–3G, with T_{EX} cells from GEO: GSE188670. (C) UMAP projection of T_{RM} and T_{EX} cells based on scATAC-seq analysis. (D) UMAP depicting *Itgae*, *Cx3cr1*, *Cxcr6*, *Havcr2*, *Tcf7*, and *Pdcd1* gene scores. (E) T_{RM}, $T_{EX\text{-}PROG}$, $T_{EX\text{-}INT}$, and $T_{EX\text{-}TERM}$ cell peak signatures in indicated clusters. (F) Heatmap identifying $T_{EX\text{-}TERM}$ and T_{RM} cell shared and exclusive peaks. (G) *Pdcd1* genome tracks of cluster aggregated scATAC-seq data (height normalized). (H) Heatmap of TF motif (The Encyclopedia of DNA Elements, ENCODE) enrichment in the marker peaks of indicated populations.

peaks in T_{EX} cells may contribute to the phenotypic and functional similarities between the cell subsets; however, $T_{EX\text{-}TERM}$ cells are defined by a much greater number of T_{EX} cell-specific peaks, largely absent in T_{RM} cells.

Understanding the differentiation regulation of T_{RM} cells is critical to inform the design of therapies that aim to modulate tissue immunity. Our data indicate that memory T cell subsets are epigenetically distinct and that each may arise from epigenetically poised precursors generated early after infection.[54] Our resource will provide extensive opportunities for additional investigation of epigenetic regulators involved in T_{RM}, T_{CIRC}, and T_{EX} cell differentiation.

Limitations of the study

Our study has relied on the use of TCR transgenic $CD8^+$ T cells, each specifically designed to recognize a single epitope. Although transgenic T cells are widely used to exclude the highly diverse T cell repertoire as a confounding factor, they may not fully replicate the diverse nature of endogenous T cell responses triggered during natural infections. Furthermore, we acknowledge the limitations of ATAC-seq. When assessing TF activity, it is important to note that TF motif databases utilize a combination of experimentally and computationally derived binding motifs, which may vary in reliability. Additionally, distinguishing between TFs within the same family or other TFs that share a common DNA binding motif is challenging, highlighting the need for careful interpretation and experimental validation.

STAR★METHODS

Detailed methods are provided in the online version of this paper and include the following:

- KEY RESOURCES TABLE
- RESOURCE AVAILABILITY
  - Lead contact
  - Materials availability
  - Data and code availability
- EXPERIMENTAL MODELS AND STUDY PARTICIPANT DETAILS
  - Mice
- METHOD DETAILS
  - Adoptive cell transfers, infections and DNFB
  - Organ processing
  - Flow cytometry and cell sorting
  - CRISPR-Cas9 Editing
  - Multiome
  - scATAC-seq
- QUANTIFICATION AND STATISTICAL ANALYSIS

SUPPLEMENTAL INFORMATION

Supplemental information can be found online at https://doi.org/10.1016/j.immuni.2024.06.014.

ACKNOWLEDGMENTS

The authors thank the Flow Cytometry Unit and Bioresources Facility at Peter Doherty Institute (University of Melbourne) and the Stanford Functional Genomics Facility. This work was supported by Institutional Training Grant 5T32AI007290 (F.A.B.); ARC DECRA DE220100165 (R.F.); HHMI-Gates International Research Scholarship OPP1175796, NHMRC AP1113293, and Sylvia and Charles Viertel SMRF (L.K.M.); and NIH U01CA260852, the Parker Institute for Cancer Immunotherapy, a Lloyd J. Old STAR award from the Cancer Research Institute, a Career Award for Medical Scientists from the Burroughs Welcome Fund, a Pew-Stewart Scholars for Cancer Research Award, and a CRISPR Cures for Cancer Initiative Award (A.T.S.).

AUTHOR CONTRIBUTIONS

F.A.B., R.F., P.K.Y., F.W., M.E., A.O., J.C.G., C.J.R., J.A.B., B.D., K.E.Y., Y.Q., Y.Y., K.F.N., F.M.T., and C.A.L. performed experiments and analyzed data. M.R.H., A.T.S., and L.K.M. provided supervision. F.A.B., R.F., A.T.S., and L.K.M. contributed to experimental design. F.A.B., R.F., P.Z., P.K.Y., A.T.S., and L.K.M. prepared the manuscript. A.T.S. and L.K.M. provided funding and led the research program.

DECLARATION OF INTERESTS

A.T.S. is a founder of Immunai, Cartography Biosciences, Santa Ana Bio, and Prox Biosciences and receives research funding from Merck Research Laboratories, Allogene Therapeutics, and Astellas Pharma. K.E.Y. is a consultant for Cartography Biosciences.

Received: December 18, 2023
Revised: May 7, 2024
Accepted: June 27, 2024
Published: July 22, 2024

REFERENCES

1. Masopust, D., and Soerens, A.G. (2019). Tissue-Resident T Cells and Other Resident Leukocytes. Annu. Rev. Immunol. *37*, 521–546.
2. Szabo, P.A., Miron, M., and Farber, D.L. (2019). Location, location, location: Tissue resident memory T cells in mice and humans. Sci. Immunol. *4*, 1–12.
3. Christo, S.N., Evrard, M., Park, S.L., Gandolfo, L.C., Burn, T.N., Fonseca, R., Newman, D.M., Alexandre, Y.O., Collins, N., Zamudio, N.M., et al. (2021). Discrete tissue microenvironments instruct diversity in resident memory T cell function and plasticity. Nat. Immunol. *22*, 1140–1151.
4. Mackay, L.K., Minnich, M., Kragten, N.A.M., Liao, Y., Nota, B., Seillet, C., Zaid, A., Man, K., Preston, S., Freestone, D., et al. (2016). Hobit and Blimp1 instruct a universal transcriptional program of tissue residency in lymphocytes. Science *352*, 459–463.
5. Kumar, B.V., Ma, W., Miron, M., Granot, T., Guyer, R.S., Carpenter, D.J., Senda, T., Sun, X., Ho, S.H., Lerner, H., et al. (2017). Human Tissue-Resident Memory T Cells Are Defined by Core Transcriptional and Functional Signatures in Lymphoid and Mucosal Sites. Cell Rep. *20*, 2921–2934.
6. Beura, L.K., Wijeyesinghe, S., Thompson, E.A., Macchietto, M.G., Rosato, P.C., Pierson, M.J., Schenkel, J.M., Mitchell, J.S., Vezys, V., Fife, B.T., et al. (2018). T Cells in Nonlymphoid Tissues Give Rise to Lymph-Node-Resident Memory T Cells. Immunity *48*, 327–338.e5.
7. Masopust, D., Choo, D., Vezys, V., Wherry, E.J., Duraiswamy, J., Akondy, R., Wang, J., Casey, K.A., Barber, D.L., Kawamura, K.S., et al. (2010). Dynamic T cell migration program provides resident memory within intestinal epithelium. J. Exp. Med. *207*, 553–564.
8. Joshi, N.S., Cui, W., Chandele, A., Lee, H.K., Urso, D.R., Hagman, J., Gapin, L., and Kaech, S.M. (2007). Inflammation Directs Memory Precursor and Short-Lived Effector CD8+ T Cell Fates via the Graded Expression of T-bet Transcription Factor. Immunity *27*, 281–295.
9. Sarkar, S., Kalia, V., Haining, W.N., Konieczny, B.T., Subramaniam, S., and Ahmed, R. (2008). Functional and genomic profiling of effector CD8 T cell subsets with distinct memory fates. J. Exp. Med. *205*, 625–640.
10. Solouki, S., Huang, W., Elmore, J., Limper, C., Huang, F., and August, A. (2020). TCR Signal Strength and Antigen Affinity Regulate CD8 + Memory T Cells. J. Immunol. *205*, 1217–1227.
11. Evrard, M., Becht, E., Fonseca, R., Obers, A., Park, S.L., Ghabdan-Zanluqui, N., Schroeder, J., Christo, S.N., Schienstock, D., Lai, J., et al.

(2023). Single-cell protein expression profiling resolves circulating and resident memory T cell diversity across tissues and infection contexts. Immunity *56*, 1664–1680.e9.

12. Milner, J.J., Toma, C., He, Z., Kurd, N.S., Nguyen, Q.P., McDonald, B., Quezada, L., Widjaja, C.E., Witherden, D.A., Crowl, J.T., et al. (2020). Heterogenous Populations of Tissue-Resident CD8+ T Cells Are Generated in Response to Infection and Malignancy. Immunity *52*, 808–824.e7.
13. Jameson, S.C., and Masopust, D. (2009). Diversity in T Cell Memory: An Embarrassment of Riches. Immunity *31*, 859–871.
14. Paik, D.H., and Farber, D.L. (2021). Anti-viral protective capacity of tissue resident memory T cells. Curr. Opin. Virol. *46*, 20–26.
15. Heeg, M., and Goldrath, A.W. (2023). Insights into phenotypic and functional CD8+ TRM heterogeneity. Immunol. Rev. *316*, 8–22.
16. Miller, B.C., Sen, D.R., Al Abosy, R., Bi, K., Virkud, Y.V., LaFleur, M.W., Yates, K.B., Lako, A., Felt, K., Naik, G.S., et al. (2019). Subsets of exhausted CD8+ T cells differentially mediate tumor control and respond to checkpoint blockade. Nat. Immunol. *20*, 326–336.
17. Paley, M.A., Kroy, D.C., Odorizzi, P.M., Johnnidis, J.B., Dolfi, D.V., Barnett, B.E., Bikoff, E.K., Robertson, E.J., Lauer, G.M., Reiner, S.L., et al. (2012). Progenitor and terminal subsets of CD8+ T cells cooperate to contain chronic viral infection. Science *338*, 1220–1225.
18. Im, S.J., Hashimoto, M., Gerner, M.Y., Lee, J., Kissick, H.T., Burger, M.C., Shan, Q., Hale, J.S., Lee, J., Nasti, T.H., et al. (2016). Defining $CD8^+$ T cells that provide the proliferative burst after PD-1 therapy. Nature *537*, 417–421.
19. McLane, L.M., Abdel-Hakeem, M.S., and Wherry, E.J. (2019). CD8 T Cell Exhaustion During Chronic Viral Infection and Cancer. Annu. Rev. Immunol. *37*, 457–495.
20. Mackay, L.K., Wakim, L., van Vliet, C.J., Jones, C.M., Mueller, S.N., Bannard, O., Fearon, D.T., Heath, W.R., and Carbone, F.R. (2012). Maintenance of T Cell Function in the Face of Chronic Antigen Stimulation and Repeated Reactivation for a Latent Virus Infection. J. Immunol. *188*, 2173–2178.
21. Chang, J.T., Wherry, E.J., and Goldrath, A.W. (2014). Molecular regulation of effector and memory T cell differentiation. Nat. Immunol. *15*, 1104–1115.
22. Milner, J.J., and Goldrath, A.W. (2018). Transcriptional programming of tissue-resident memory $CD8^+$ T cells. Curr. Opin. Immunol. *51*, 162–169.
23. Dogra, P., Ghoneim, H.E., Abdelsamed, H.A., and Youngblood, B. (2016). Generating long-lived $CD8^+$ T-cell memory: Insights from epigenetic programs. Eur. J. Immunol. *46*, 1548–1562.
24. Araki, K., Turner, A.P., Shaffer, V.O., Gangappa, S., Keller, S.A., Bachmann, M.F., Larsen, C.P., and Ahmed, R. (2009). mTOR regulates memory CD8 T-cell differentiation. Nature *460*, 108–112.
25. Scharer, C.D., Barwick, B.G., Youngblood, B.A., Ahmed, R., and Boss, J.M. (2013). Global DNA Methylation Remodeling Accompanies CD8 T Cell Effector Function. J. Immunol. *191*, 3419–3429.
26. Akondy, R.S., Fitch, M., Edupuganti, S., Yang, S., Kissick, H.T., Li, K.W., Youngblood, B.A., Abdelsamed, H.A., McGuire, D.J., Cohen, K.W., et al. (2017). Origin and differentiation of human memory CD8 T cells after vaccination. Nature *552*, 362–367.
27. Satpathy, A.T., Granja, J.M., Yost, K.E., Qi, Y., Meschi, F., McDermott, G.P., Olsen, B.N., Mumbach, M.R., Pierce, S.E., Corces, M.R., et al. (2019). Massively parallel single-cell chromatin landscapes of human immune cell development and intratumoral T cell exhaustion. Nat. Biotechnol. *37*, 925–936.
28. Lareau, C.A., Duarte, F.M., Chew, J.G., Kartha, V.K., Burkett, Z.D., Kohlway, A.S., Pokholok, D., Aryee, M.J., Steemers, F.J., Lebofsky, R., et al. (2019). Droplet-based combinatorial indexing for massive-scale single-cell chromatin accessibility. Nat. Biotechnol. *37*, 916–924.
29. Granja, J.M., Corces, M.R., Pierce, S.E., Bagdatli, S.T., Choudhry, H., Chang, H.Y., and Greenleaf, W.J. (2021). ArchR is a scalable software package for integrative single-cell chromatin accessibility analysis. Nat. Genet. *53*, 403–411.
30. Becht, E., McInnes, L., Healy, J., Dutertre, C.A., Kwok, I.W.H., Ng, L.G., Ginhoux, F., and Newell, E.W. (2018). Dimensionality reduction for visualizing single-cell data using UMAP. Nat. Biotechnol. *37*, 38–47.
31. Cusanovich, D.A., Daza, R., Adey, A., Pliner, H.A., Christiansen, L., Gunderson, K.L., Steemers, F.J., Trapnell, C., and Shendure, J. (2015). Multiplex single cell profiling of chromatin accessibility by combinatorial cellular indexing. Science *348*, 910–914.
32. Pliner, H.A., Packer, J.S., McFaline-Figueroa, J.L., Cusanovich, D.A., Daza, R.M., Aghamirzaie, D., Srivatsan, S., Qiu, X., Jackson, D., Minkina, A., et al. (2018). Cicero Predicts cis-Regulatory DNA Interactions from Single-Cell Chromatin Accessibility Data. Mol. Cell *71*, 858–871.e8.
33. Sumida, H., Lu, E., Chen, H., Yang, Q., Mackie, K., and Cyster, J.G. (2017). GPR55 regulates intraepithelial lymphocyte migration dynamics and susceptibility to intestinal damage. Sci. Immunol. *2*, 1–16.
34. Boulay, G., Dubuissez, M., Van Rechem, C., Forget, A., Helin, K., Ayrault, O., and Leprince, D. (2012). Hypermethylated in cancer 1 (HIC1) recruits polycomb repressive complex 2 (PRC2) to a subset of its target genes through interaction with human polycomb-like (hPCL) proteins. J. Biol. Chem. *287*, 10509–10524.
35. Crowl, J.T., Heeg, M., Ferry, A., Milner, J.J., Omilusik, K.D., Toma, C., He, Z., Chang, J.T., and Goldrath, A.W. (2022). Tissue-resident memory CD8+ T cells possess unique transcriptional, epigenetic and functional adaptations to different tissue environments. Nat. Immunol. *23*, 1121–1131.
36. Klein, K., Witalisz-Siepracka, A., Gotthardt, D., Agerer, B., Locker, F., Grausenburger, R., Knab, V.M., Bergthaler, A., and Sexl, V. (2021). T Cell-Intrinsic CDK6 Is Dispensable for Anti-Viral and Anti-Tumor Responses In Vivo. Front. Immunol. *12*, 650977.
37. Lingel, H., Wissing, J., Arra, A., Schanze, D., Lienenklaus, S., Klawonn, F., Pierau, M., Zenker, M., Jänsch, L., and Brunner-Weinzierl, M.C. (2017). CTLA-4-mediated posttranslational modifications direct cytotoxic T-lymphocyte differentiation. Cell Death Differ. *24*, 1739–1749.
38. Kurd, N.S., He, Z., Louis, T.L., Milner, J.J., Omilusik, K.D., Jin, W., Tsai, M.S., Widjaja, C.E., Kanbar, J.N., Olvera, J.G., et al. (2020). Early precursors and molecular determinants of tissue-resident memory $CD8^+$ T lymphocytes revealed by single-cell RNA sequencing. Sci. Immunol. *5*, eaaz6894.
39. Milner, J.J., Toma, C., Yu, B., Zhang, K., Omilusik, K., Phan, A.T., Wang, D., Getzler, A.J., Nguyen, T., Crotty, S., et al. (2017). Runx3 programs CD8+ T cell residency in non-lymphoid tissues and tumours. Nature *552*, 253–257.
40. Kok, L., Dijkgraaf, F.E., Urbanus, J., Bresser, K., Vredevoogd, D.W., Cardoso, R.F., Perié, L., Beltman, J.B., and Schumacher, T.N. (2020). A committed tissue-resident memory T cell precursor within the circulating CD8+ effector T cell pool. J. Exp. Med. *217*, e20191711.
41. Hao, Y., Hao, S., Andersen-Nissen, E., Mauck, W.M., Zheng, S., Butler, A., Lee, M.J., Wilk, A.J., Darby, C., Zager, M., et al. (2021). Integrated analysis of multimodal single-cell data. Cell *184*, 3573–3587.e29.
42. Mimitou, E.P., Lareau, C.A., Chen, K.Y., Zorzetto-Fernandes, A.L., Hao, Y., Takeshima, Y., Luo, W., Huang, T.S., Yeung, B.Z., Papalexi, E., et al. (2021). Scalable, multimodal profiling of chromatin accessibility, gene expression and protein levels in single cells. Nat. Biotechnol. *39*, 1246–1258.
43. Morris, A.B., Farley, C.R., Pinelli, D.F., Adams, L.E., Cragg, M.S., Boss, J.M., Scharer, C.D., Fribourg, M., Cravedi, P., Heeger, P.S., et al. (2020). Signaling through the Inhibitory Fc Receptor FcγRIIB Induces CD8+ T Cell Apoptosis to Limit T Cell Immunity. Immunity *52*, 136–150.e6.
44. Zhou, X., Yu, S., Zhao, D.M., Harty, J.T., Badovinac, V.P., and Xue, H.H. (2010). Differentiation and Persistence of Memory $CD8^+$ T Cells Depend on T Cell Factor 1. Immunity *33*, 229–240.

45. Park, S.L., and Mackay, L.K. (2021). Decoding tissue-residency: Programming and potential of frontline memory T cells. Cold Spring Harb. Perspect. Biol. *13*, a037960.

46. Hirai, T., Yang, Y., Zenke, Y., Li, H., Chaudhri, V.K., De La Cruz Diaz, J.S., Zhou, P.Y., Nguyen, B.A.T., Bartholin, L., Workman, C.J., et al. (2021). Competition for Active TGFβ Cytokine Allows for Selective Retention of Antigen-Specific Tissue- Resident Memory T Cells in the Epidermal Niche. Immunity *54*, 84–98.e5.

47. Mackay, L.K., Rahimpour, A., Ma, J.Z., Collins, N., Stock, A.T., Hafon, M.L., Vega-Ramos, J., Lauzurica, P., Mueller, S.N., Stefanovic, T., et al. (2013). The developmental pathway for CD103^{+} CD8^{+} tissue-resident memory T cells of skin. Nat. Immunol. *14*, 1294–1301.

48. Holz, L.E., Chua, Y.C., de Menezes, M.N., Anderson, R.J., Draper, S.L., Compton, B.J., Chan, S.T.S., Mathew, J., Li, J., Kedzierski, L., et al. (2020). Glycolipid-peptide vaccination induces liver-resident memory CD8+ T cells that protect against rodent malaria. Sci. Immunol. *5*, 1–14.

49. Frizzell, H., Fonseca, R., Christo, S.N., Evrard, M., Cruz-Gomez, S., Zanluqui, N.G., von Scheidt, B., Freestone, D., Park, S.L., McWilliam, H.E.G., et al. (2020). Organ-specific isoform selection of fatty acid-binding proteins in tissue-resident lymphocytes. Sci. Immunol. *5*, eaay9283.

50. Zhang, Y., Feng, X.H., and Derynck, R. (1998). Smad3 and Smad4 cooperate with c-Jun/c-Fos to mediate TGF-beta-induced transcription. Nature *394*, 909–913.

51. Park, S.L., Christo, S.N., Wells, A.C., Gandolfo, L.C., Zaid, A., Alexandre, Y.O., Burn, T.N., Schröder, J., Collins, N., Han, S.-J., et al. (2023). Divergent molecular networks program functionally distinct CD8+ skin-resident memory T cells. Science *382*, 1073–1079.

52. Li, C., Zhu, B., Son, Y.M., Wang, Z., Jiang, L., Xiang, M., Ye, Z., Beckermann, K.E., Wu, Y., Jenkins, J.W., et al. (2019). The Transcription Factor Bhlhe40 Programs Mitochondrial Regulation of Resident CD8+ T Cell Fitness and Functionality. Immunity *51*, 491–507.e7.

53. Baxter, A.E., Huang, H., Giles, J.R., Chen, Z., Wu, J.E., Drury, S., Dalton, K., Park, S.L., Torres, L., Simone, B.W., et al. (2023). The SWI/SNF chromatin remodeling complexes BAF and PBAF differentially regulate epigenetic transitions in exhausted CD8^{+} T cells. Immunity *56*, 1320–1340.e10.

54. McDonald, B., Chick, B.Y., Ahmed, N.S., Burns, M., Ma, S., Casillas, E., Chen, D., Mann, T.H., O'Connor, C., Hah, N., et al. (2023). Canonical BAF complex activity shapes the enhancer landscape that licenses CD8^{+} T cell effector and memory fates. Immunity *56*, 1303–1319.e5.

55. Man, K., Gabriel, S.S., Liao, Y., Gloury, R., Preston, S., Henstridge, D.C., Pellegrini, M., Zehn, D., Berberich-Siebelt, F., Febbraio, M.A., et al. (2017). Transcription Factor IRF4 Promotes CD8+ T Cell Exhaustion and Limits the Development of Memory-like T Cells during Chronic. Infect. Immun. *47*, 1129–1141.e5.

56. Sen, D.R., Kaminski, J., Barnitz, R.A., Kurachi, M., Gerdemann, U., Yates, K.B., Tsao, H.W., Godec, J., LaFleur, M.W., Brown, F.D., et al. (2016). The epigenetic landscape of T cell exhaustion. Science *354*, 1165–1169.

57. Philip, M., Fairchild, L., Sun, L., Horste, E.L., Camara, S., Shakiba, M., Scott, A.C., Viale, A., Lauer, P., Merghoub, T., et al. (2017). Chromatin states define tumour-specific T cell dysfunction and reprogramming. Nature *545*, 452–456.

58. Beltra, J.C., Manne, S., Abdel-Hakeem, M.S., Kurachi, M., Giles, J.R., Chen, Z., Casella, V., Ngiow, S.F., Khan, O., Huang, Y.J., et al. (2020). Developmental Relationships of Four Exhausted CD8+ T Cell Subsets Reveals Underlying Transcriptional and Epigenetic Landscape Control Mechanisms. Immunity *52*, 825–841.e8.

59. Giles, J.R., Manne, S., Freilich, E., Huang, A.C., Shi, J., and Wherry, E.J. (2022). Resource Human epigenetic and transcriptional T cell differentiation atlas for identifying functional T cell- specific enhancers. Immunity *55*, 557–574.e7.

60. Daniel, B., Yost, K.E., Hsiung, S., Sandor, K., Xia, Y., Qi, Y., Hiam-Galvez, K.J., Black, M., J Raposo, C., Shi, Q., et al. (2022). Divergent clonal differentiation trajectories of T cell exhaustion. Nat. Immunol. *23*, 1614–1627.

61. Raju, S., Xia, Y., Daniel, B., Yost, K.E., Bradshaw, E., Tonc, E., Verbaro, D.J., Kometani, K., Yokoyama, W.M., Kurosaki, T., et al. (2021). Identification of a T-bet^{hi} Quiescent Exhausted CD8 T Cell Subpopulation That Can Differentiate into TIM3^{+} CX3CR1^{+} Effectors and Memory-like Cells. J. Immunol. *206*, 2924–2936.

62. Pauken, K.E., Sammons, M.A., Odorizzi, P.M., Manne, S., Godec, J., Khan, O., Drake, A.M., Chen, Z., Sen, D.R., Kurachi, M., et al. (2016). Epigenetic stability of exhausted T cells limits durability of reinvigoration by PD-1 blockade. Science *354*, 1160–1165.

63. Khan, O., Giles, J.R., Mcdonald, S., Manne, S., Ngiow, S.F., Patel, K.P., Werner, M.T., Huang, A.C., Alexander, K.A., Wu, J.E., et al. (2019). TOX transcriptionally and epigenetically programs CD8+ T cell exhaustion. Nature *571*, 211–218.

64. Scott, A.C., Dündar, F., Zumbo, P., Chandran, S.S., Klebanoff, C.A., Shakiba, M., Trivedi, P., Menocal, L., Appleby, H., Camara, S., et al. (2019). TOX is a critical regulator of tumour-specific T cell differentiation. Nature *571*, 270–274.

65. Alfei, F., Kanev, K., Hofmann, M., Wu, M., Ghoneim, H.E., Roelli, P., Utzschneider, D.T., von Hoesslin, M., Cullen, J.G., Fan, Y., et al. (2019). TOX reinforces the phenotype and longevity of exhausted T cells in chronic viral infection. Nature *571*, 265–269.

66. Martinez, G.J., Pereira, R.M., Äijö, T., Kim, E.Y., Marangoni, F., Pipkin, M.E., Togher, S., Heissmeyer, V., Zhang, Y.C., Crotty, S., et al. (2015). The Transcription Factor NFAT Promotes Exhaustion of Activated CD8^{+} T Cells. Immunity *42*, 265–278.

67. Chen, Y., Zander, R.A., Wu, X., Schauder, D.M., Kasmani, M.Y., Shen, J., Zheng, S., Burns, R., Taparowsky, E.J., and Cui, W. (2021). BATF regulates progenitor to cytolytic effector CD8+ T cell transition during chronic viral infection. Nat. Immunol. *22*, 996–1007.

68. Roychoudhuri, R., Clever, D., Li, P., Wakabayashi, Y., Quinn, K.M., Klebanoff, C.A., Ji, Y., Sukumar, M., Eil, R.L., Yu, Z., et al. (2016). BACH2 regulates CD8^{+} T cell differentiation by controlling access of AP-1 factors to enhancers. Nat. Immunol. *17*, 851–860.

69. Yukawa, M., Jagannathan, S., Vallabh, S., Kartashov, A.V., Chen, X., Weirauch, M.T., and Barski, A. (2020). AP-1 activity induced by co-stimulation is required for chromatin opening during T cell activation. J. Exp. Med. *217*, e20182009.

70. Stuart, T., Butler, A., Hoffman, P., Hafemeister, C., Papalexi, E., Mauck, W.M., III, Hao, Y., Stoeckius, M., Smibert, P., and Satija, R. (2019). Comprehensive integration of single-cell data. Cell *177*, 1888–1902.

71. Heinz, S., Benner, C., Spann, N., Bertolino, E., Lin, Y.C., Laslo, P., Cheng, J.X., Murre, C., Singh, H., and Glass, C.K. (2010). Simple combinations of lineage-determining transcription factors prime cis-regulatory elements required for macrophage and B cell identities. Mol. Cell. *38*, 576–589.

72. Love, M.I., Huber, W., and Anders, S. (2014). Moderated estimation of fold change and dispersion for RNA-seq data with DESeq2. Genome Biol. *15*, 550.

73. Imperato, J.N., Xu, D., Romagnoli, P.A., Qiu, Z., Perez, P., Khairallah, C., Pham, Q.M., Andrusaite, A., Bravo-Blas, A., Milling, S.W.F., et al. (2020). Mucosal CD8 T Cell Responses Are Shaped by Batf3-DC After Foodborne Listeria monocytogenes Infection. Front. Immunol. *11*, 575967.

74. Mackay, L.K., Stock, A.T., Ma, J.Z., Jones, C.M., Kent, S.J., Mueller, S.N., Heath, W.R., Carbone, F.R., and Gebhardt, T. (2012). Long-lived epithelial immunity by tissue-resident memory T (TRM) cells in the absence of persisting local antigen presentation. Proc. Natl. Acad. Sci. USA *109*, 7037–7042.

75. Nüssing, S., House, I.G., Kearney, C.J., Chen, A.X.Y., Vervoort, S.J., Beavis, P.A., Oliaro, J., Johnstone, R.W., Trapani, J.A., and Parish, I.A. (2020). Efficient CRISPR/Cas9 Gene Editing in Uncultured Naive Mouse T Cells for In Vivo Studies. J. Immunol. *204*, 2308–2315.

STAR★METHODS

KEY RESOURCES TABLE

REAGENT or RESOURCE	SOURCE	IDENTIFIER
Antibodies		
Anti-CD45.1-APC/R700; Clone A20	BD Biosciences	Cat#565814; RRID: AB_2744397
Anti-CD45.1-PE/Cy7; Clone A20	Biolegend	Cat#110730; RRID: AB_1134168
Anti-CD45.2-APC; Clone 104	Biolegend	Cat#109814; RRID: AB_389211
Anti-CD45.2-SparkNIR685; Clone 104	Biolegend	Cat#109864; RRID: AB_2876424
Anti-CD8α-BV786; Clone 53-6.7	BD Biosciences	Cat# 563332; RRID: AB_2721167
Anti-CD8α-BV711; Clone 53-6.7	BD Biosciences	Cat#563046; RRID: AB_2737972
Anti-CD8β-BV750; Clone H35-17.2	BD Biosciences	Cat#747505; RRID: AB_2872172
Anti-CD8β-BV786; Clone H35-17.2	BD Biosciences	Cat#740952; RRID: AB_2740577
Anti-CD3ε-FITC; Clone 500A2	Biolegend	Cat#152305; RRID: AB_2632667
Anti-Vα2-BV421; Clone B20.1	BD Biosciences	Cat#562944; RRID: AB_2737910
Anti-Vα2-PE/Cy7; Clone B20.1	BD Biosciences	Cat#560624; RRID: AB_1727584
Anti-Vα2-BV480; Clone B20.1	BD Biosciences	Cat#746615; RRID: AB_2743895
Anti-CD44-BV510; Clone IM7	BD Biosciences	Cat#563114; RRID: AB_2738011
Anti-CD49a-BV711; Clone Ha31/8	BD Biosciences	Cat#564863; RRID: AB_2738987 Cat#742164; RRID: AB_2861198273
Anti-CD127-BV421; Clone A7R34;	Biolegend	Cat#135027; RRID: AB_2563103
Anti-CXCR6-FITC; Clone SA051D1	Biolegend	Cat#151108; RRID: AB_2572145
Anti-CXCR6-PE/Dazzle594; Clone SA051D1	Biolegend	Cat#151117; RRID: AB_2721700
Anti-CX3CR1-BV650; Clone SA011F11	Biolegend	Cat#149033; RRID: AB_2565999
Anti-CD62L-BUV737; Clone MEL-14	BD Biosciences	Cat#612833; RRID: AB_2870155
Anti-CD62L-BV605; Clone MEL-14	BD Biosciences	Cat#563252; RRID: AB_2738098
Anti-CD69-PE/Cy5; Clone H1.2F3	Biolegend	Cat#104510; RRID: AB_313113
Anti-CD103-eF450; Clone 2E7	Thermo Fisher Scientific	Cat#48-1031-82; RRID: AB_2574033
Anti-PD1-BV711; Clone 29F.1A12	Biolegend	Cat#135231; RRID: AB_2566158
Anti-Ly6C-BV785; Clone HK1.4	Biolegend	Cat#128041; RRID: AB_2565852
Anti-TCRβ-BV650; Clone H57-597	Biolegend	Cat#109251; RRID: AB_2810348
Anti-TCRβ-BV711; Clone H57-597	Biolegend	Cat#109243; RRID: AB_2629564
Anti-Tim3-APC; Clone RMT3-23	Biolegend	Cat#119706; RRID: AB_2561656
Anti-CD43-FITC; Clone 1B11	Biolegend	Cat#121206; RRID: AB_493386
Anti-Ly108-PE; Clone 330-AJ	Biolegend	Cat#134606; RRID: AB_2188095
Anti-Ly108-APC; Clone 330-AJ	Biolegend	Cat#134606; RRID: AB_2728155
Anti-CD38-BV750; Clone 90	BD Biosciences	Cat#747103; RRID: AB_2871855
Anti-CD38-PE/Cy7; Clone 90	Biolegend	Cat#102718; RRID: AB_2275531
Anti-CD32b-PE; Clone AT130-2	Thermo Fisher Scientific	Cat#12-0321-82; RRID: AB_2572557
Anti-TOX-PE; Clone TXRX10	Thermo Fisher Scientific	Cat#12-6502-82; RRID: AB_10855034
Anti-TCF1-AF488; Clone C63D9	Cell Signaling	Cat#2203S; RRID: AB_2199302
Anti-MHCII-SparkBlue550; Clone M5/114.15.2	Biolegend	Cat#107662; RRID: AB_2860616
Anti-CD73-BV421; Clone TY/11.8	Biolegend	Cat#127217; RRID: AB_2687251
Anti-CD73-BV711; Clone TY/11.8	BD Biosciences	Cat#752736; RRID: AB_2917717
Anti-LAG3-PE/Cy7; Clone C9B7W	Thermo Fisher Scientific	Cat# 25-2231-82; RRID: AB_2573428
Anti-KLRG1-APC/eF780; Clone 2F1	Thermo Fisher Scientific	Cat#47-5893-82; RRID: AB_2573988
Anti-KLRG1-PE/eF610; Clone 2F1	Thermo Fisher Scientific	Cat#61-5893-82; RRID: AB_2574630
Anti-IFNγ-BV480; Clone XMG1.2	BD Biosciences	Cat#566097; RRID: AB_2739501
Anti-TNF-BV711; Clone MP6-XT22	Biolegend	Cat#506349; RRID: AB_2629800

(*Continued on next page*)

Continued

REAGENT or RESOURCE	SOURCE	IDENTIFIER
Anti-CD3ε Purified; Clone 145-2C11	Biolegend	Cat#100302; RRID: AB_312677
Anti-CD28 Purified; Clone 37.51	Biolegend	Cat#102102; RRID: AB_312867
Bacterial and virus strains		
Herpes Simplex virus type-1 (HSV-1), KOS strain	F. Carbone, University of Melbourne	N/A
Lymphocytic choriomeningitis virus (LCMV) Armstrong strain	S. Mueller, University of Melbourne	N/A
Lymphocytic choriomeningitis virus (LCMV) Clone-13	S. Mueller, University of Melbourne	N/A
Listeria monocytogenes (Lm-OVA), InlA mutant	B. Sheridan, Stony Brook University	N/A
Influenza virus A/HKX31 (X31-OVA)	P. Doherty, University of Melbourne	N/A
Chemicals, peptides, and recombinant proteins		
Ghost Dye™ Red 780	Tonbo Bioscience	Cat#13-0865-T500
H-2D(b) LCMV GP33 biotinylated monomer (KAVYNFATM)	NIH tetramer core facility	N/A
GP33 peptide (KAVYNFATM)	Auspep	N/A
Alt-R S.p. Cas9 Nuclease V3	Integrated DNA Technologies	Cat#1081059
Collagenase type III	Worthington Biochemical	Cat#LS004183
Dispase® II (neutral protease, grade II)	Roche	Cat#4942078001
Liberase TL Research Grade	Sigma-Aldrich	Cat#5401020001
DNase I	Roche	Cat#10104159001
Percoll	Thermo Fisher Scientific	Cat#GE17-0891-01
1,4-Dithioerythritol	Sigma-Aldrich	Cat#D8255
10X HBSS, no Ca^{2+}, no Mg^{2+}	Thermo Fisher Scientific	Cat#14180046
eBioscience 1X RBC Lysis Buffer	Thermo Fisher Scientific	Cat#00-4333-57
Brefeldin A from Penicillium	Sigma-Aldrich	Cat#B6542
Human recombinant IL-2	Peprotech	Cat#200-02
Bovine serum albumin	Sigma-Aldrich	Cat#A7906
EDTA	Sigma-Aldrich	Cat#E5134
Fetal Bovine serum	Sigma-Aldrich	Cat#12007C
2-Mercaptoethanol	Sigma-Aldrich	Cat#M3148
Penicillin/Streptomycin	Sigma-Aldrich	Cat#P0781
L-Glutamine	Sigma-Aldrich	Cat# G8540
RPMI	In house	N/A
HEPES	Sigma-Aldrich	Cat#H3375
BioMag Goat Anti-Rat IgG	Qiagen	Cat#310107
PKH26 Reference Microbeads	Sigma-Aldrich	Cat#P7458
Acetone	Sigma-Aldrich	Cat#179124
Sunflower seed oil	Sigma-Aldrich	Cat#S5007
DMEM	In house	N/A
Lipofectamine 3000	Thermo Fisher Scientific	Cat#L3000150
Tween-20	Promega	Cat#H5152
Digitonin	Sigma-Aldrich	Cat#300410
DTT	Sigma-Aldrich	Cat#A39255
TheraPure™ GMP RNase Inhibitor, 40 U/μL	Thermo Fisher Scientific	Cat#EO038SKB011

(*Continued on next page*)

Continued

REAGENT or RESOURCE	SOURCE	IDENTIFIER
Critical commercial assays		
BD Cytofix/Cytoperm Fixation/ Permeabilization Kit	BD Bioscience	Cat#554714; RRID: AB_2869008
eBioscience FoxP3/Transcription Factor Staining Buffer Set	Thermo Fisher Scientific	Cat#00-5523-00
P3 Primary Cell 4D-NucleofectorTM X Kit S	Lonza	Cat#V4XP-3032
NovaSeq 6000 S4 Reagent kit	Illumina	Cat#20028312
Chromium Next GEM Single Cell Multiome ATAC + Gene Expression Reagent Kit	10x Genomics	Cat#1000283
Chromium Single Cell V(D)J Enrichment Kit	10x Genomics	Cat#PN-1000071
Chromium Single Cell ATAC Reagent Kit	10x Genomics	Cat#1000390
Chromium Single Cell 5′ Library Construction Kit	10x Genomics	Cat#PN-1000020
Chromium Next GEM Single Cell 5′ Library and Gel Bead Kit v1.1	10x Genomics	Cat#PN-1000165
Chromium Next GEM Single Cell ATAC Library & Gel Bead Kit, 16 rxns	10x Genomics	Cat#PN-1000175
Deposited data		
GEO: GSE243597	This paper	www.ncbi.nlm.nih.gov/geo/query/acc.cgi?acc=GSE243597
GEO: GSE188670	Daniel et al.[60]	https://www.ncbi.nlm.nih.gov/geo/query/acc.cgi?acc=GSE188670
GEO: GSE70813	Mackay et al.[4]	https://www.ncbi.nlm.nih.gov/geo/query/acc.cgi?acc=GSE70813
GEO: GSE84820	Man et al.[55]	https://www.ncbi.nlm.nih.gov/geo/query/acc.cgi?acc=GSE84820
Experimental models: Organisms/strains		
Mouse: C57BL/6J	The Jackson Laboratory	Strain #:000664; RRID: IMSR_JAX:000664
Mouse: B6;D2-Tg(TcrLCMV)327Sdz/JDvsJ (P14)	The Jackson Laboratory	Strain #:004694; RRID:IMSR_JAX:004694
Mouse: C57BL/6-Tg(TcraTcrb)1100Mjb/J (OT-I)	The Jackson Laboratory	Strain #:003831; RRID:IMSR_JAX:003831
Mouse: B6.SJL-*Ptprc*^{a} *Pepc*^{b}/BoyJ (CD45.1)	The Jackson Laboratory	Strain #:002014; RRID:IMSR_JAX:002014
Mouse: B6.Tg(TcraHsv2.3,TcrbHsv2.3)L118-1Cbn (gBT-I)	S. Mueller, University of Melbourne	N/A
Oligonucleotides		
CD19 (sg*Ctrl*) (5'-AAUGUCUCAGACCAUAUGGG-3')	Synthego	N/A
Hic1 (5'-AGUGUGCGGAAAGCGCGGAG-3', 5'-CUUGUGCGACGUGAUCAUCG-3')	Synthego	N/A
Fos (5'-TGTCACCGTGGGGATAAAGTTGG-3', 5'-GGTCTGCGATGGGGCCACGGAGG-3′′)	Synthego	N/A
Fosb (5'-AGACAGGTACTGAGACTCGGCGG-3', 5'-GTTGACCCTTATGACATGCCAGG-3')	Synthego	N/A
Fosl1 (5'-GGAACCGGGACCGAGCTCCGGGG-3', 5'-GCTGCGCGGGGCGACCGTACGGG-3')	Synthego	N/A
Fosl2 (5'-GACGAGGTGTCAAAGTTCCCGGG-3', 5'-GGACATGGAGGTGATCACTGTGG-3')	Synthego	N/A
Bach2 (5'-TGCGCAGGAACTCAGCACAGCGG-3', 5'-GATGTTGGCACAGTGGACTGTGG-3')	Synthego	N/A
Fcgr2b (5'-GCCGTTCCTACTGATCCCCA-3', 5'-TCTACCCAGTGGTTCCACAA-3')	Synthego	N/A

(*Continued on next page*)

Continued

REAGENT or RESOURCE	SOURCE	IDENTIFIER
Software and algorithms		
FlowJo v10	Tree Star	https://www.flowjo.com/
Prism v9	GraphPad	https://www.graphpad.com/
OMIQ	Dotmatics	https://www.omiq.ai/
R v3.6.1	The R Project	https://www.r-project.org/
ArchR v1.0.1	Granja et al.[29]	https://www.nature.com/articles/s41587-019-0332-7
Seurat v3.11	Stuart et al., 2019[70]	https://satijalab.org/seurat
Cell Ranger ATAC v1.2.0	10x Genomics	https://support.10xgenomics.com/single-cell-atac/software
Cell Ranger v3.1.0	10x Genomics	https://support.10xgenomics.com/single-cell-vdj/software
HOMER v4.11	Heinz et al., 2010[71]	http://homer.ucsd.edu/homer/motif/
DESeq2 v3.18	Love et al.[72]	https://bioconductor.org/packages/release/bioc/html/DESeq2.html

RESOURCE AVAILABILITY

Lead contact

Further information and requests for resources and reagents should be directed to and will be fulfilled by Laura Mackay (lkmackay@unimelb.edu.au) upon request.

Materials availability

This study did not generate new unique reagents.

Data and code availability

All data have been deposited at GEO:GSE243597 and are publicly available as of the date of publication. Accession numbers are listed in the key resources table. This paper does not report original code. Any additional information required to reanalyse the data reported in this paper is available from the lead contact upon request. Public genome browsers for interrogating the chromatin accessibility profiles of $CD8^+$ T cells can be accessed using the URLs below.

For effector and memory T cells: https://epigenomegateway.wustl.edu/browser/?genome=mm10&sessionFile=https://satpathy-public-data.s3.us-west-1.amazonaws.com/buquicchio_et_al/rev/mult/Fig2.json

For T_{RM} and T_{EX} cells: https://epigenomegateway.wustl.edu/browser/?genome=mm10&sessionFile=https://satpathy-public-data.s3.us-west-1.amazonaws.com/buquicchio_et_al/rev/Fig7.json

EXPERIMENTAL MODELS AND STUDY PARTICIPANT DETAILS

Mice

C57BL/6 (RRID: IMSR_JAX:000664), C57BL/6-gBT-I, C57BL/6-Tg(TcraTcrb)1100Mjb/J (OT-I, RRID:IMSR_JAX:003831) and C57BL/6-Tg(TcrLCMV)327Sdz/JDvsJ (P14, RRID:IMSR_JAX:004694) mice were crossed with B6.SJL-*Ptprc*^{a} *Pepc*^{b}/BoyJ (CD45.1, RRID:IMSR_JAX:002014) mice and bred at the University of Melbourne or at the Stanford University. Mice were kept under a 12 h/12 h light/dark cycle, at 19–22 °C and 40–70% humidity. Six- to twelve-week-old female C56BL/6 mice were used for experiments. All experiments were approved by the University of Melbourne Animal Ethics Committee or the Stanford University Institutional Animal Care and Use Committee.

METHOD DETAILS

Adoptive cell transfers, infections and DNFB

Naïve T cells were isolated from lymph nodes and 5×10^4 cells transferred intravenously (i.v.) to C57BL/6 mice. Skin infections were performed by skin scarification with 1×10^6 plaque-forming units (PFU) of HSV-1 KOS. LCMV Armstrong infection was performed by intraperitoneal (i.p.) injection of 2×10^5 PFU and LCMV clone-13 infection via i.v. injection of 1×10^6 PFU. Lm. Lm-OVA was kindly provided by B. Sheridan (Stony Brook University) and infections performed via oral feeding as described.[73] Influenza-OVA infection was performed by intranasal (i.n.) administration of 10^4 PFU of the A/HKX31 (H3N2) strain. For treatment with 1-Fluoro-2,4-dinitrobenzene (DNFB), 15 μl of DNFB (Sigma-Aldrich) diluted at 0.25% in acetone:oil (4:1) was applied on the skin as described.[74]

Organ processing

Spleens were processed through metal meshes into single-cell suspensions followed by red blood cell lysis. Skin samples were excised and incubated at 37°C for 90 min in dispase (2.5 mg/ml; Roche) and for 30 min in collagenase III (3 mg/ml; Worthington) or liberase (0.25 mg/ml; Sigma). Liver samples were excised and meshed into single-cell suspensions, leukocytes were isolated using Percoll (35%; Sigma Aldrich). Small intestines were cut longitudinally and in 1cm fragments, incubated at 37°C for 30min with lateral rotation (230rpm) in 10% Hanks' balanced salt solution/HEPES containing dithioerythritol (0.15mg/mL; Sigma Aldrich). SG, FRT, kidneys and lungs were collected in Collagenase III (3mg/mL) with DNase I (5μg/mL; Roche), chopped and incubated for 45 min at 37°C. Lymphocytes were purified using Percoll (44/70%).

Flow cytometry and cell sorting

Cells were stained with conjugated antibodies. For intracellular staining of cytokines and TFs, cells were fixed and permeabilized using the Foxp3 TF Staining buffer set (Invitrogen) as per manufacturer's instructions. The following antibodies from BD Biosciences, Biolegend, Cell signaling or Thermo Fisher Scientific were used: anti-CD45.1 (A20), anti-CD45.2 (104), anti-CD8α (53-6.7), anti-CD8α (53-6.7), anti-CD8β (H35-17.2), anti-CD3 (500A2), anti-Vα2 (B20.1), anti-CD44 (IM7), anti-CD127 (A7R34), anti-CXCR6 (SA051D1), anti-CX3CR1 (SA011F11), anti-CD62L (MEL-14), anti-CD69 (H1.2F3), anti-CD103 (2E7), anti-PD-1 (29F.1A12), anti-Ly6C (HK1.4), anti-TCRβ (H57-597), anti-TIM-3 (RMT3-23), anti-CD43 (1B11), anti-Ly108 (330-AJ), anti-CD38 (90), anti-CD49a (Hma1), anti-CD32b (AT130-2), anti-TOX (TXRX10), anti-TCF1 (C63D9), anti-MHC-II (M5/114.15.2), anti-CD73 (TY/11.8), anti-LAG3 (C9B7W), anti-KLRG1 (2F1), anti-IFNγ (XMG1.2), anti-TNFα (MP6-XT22). Cell viability was determined using Ghost Dye Red 780 (Tonbo Biosciences). Flow cytometry was performed on an Aurora (Cytek) and analyzed with FlowJo (TreeStar) or OMIQ. Cell sorting experiments used a FACSAria III (BD Biosciences).

CRISPR-Cas9 Editing

sgRNAs targeting: *CD19* (sg*Ctrl*) (5'-AAUGUCUCAGACCAUAUGGG-3'), *Hic1* (5'-AGUGUGCGGAAAGCGCGGAG-3', 5'-CUUGUGCGACGUGAUCAUCG-3'), *Fos* (5'-TGTCACCGTGGGGATAAAGTTGG-3', 5'-GGTCTGCGATGGGGCCACGGAGG-3'), *Fosb* (5'-AGACAGGTACTGAGACTCGGCGG-3', 5'-GTTGACCCTTATGACATGCCAGG-3'), *Fosl1* (5'-GGAACCGGGACCGAGCTCCGGGG-3', 5'-GCTGCGCGGGGCGACCGTACGGG-3'), *Fosl2* (5'-GACGAGGTGTCAAAGTTCCCGGG-3', 5'-GGACATGGAGGTGATCACTGTGG-3'), *Bach2* (5'-TGCGCAGGAACTCAGCACAGCGG-3', 5'-GATGTTGGCACAGTGGACTGTGG-3'), *Fcgr2b* (5'-GCCGTTCCTACTGATCCCCA-3', 5'-TCTACCCAGTGGTTCCACAA-3') were purchased from Synthego. sgRNA/Cas9 RNPs were formed by incubating 0.3nmol of sgRNA with 0.6 ml Alt-R S.p. Cas9 nuclease V3 (10 mg/ml; Integrated DNA Technologies) for 10 min at RT. P14 T cells were *in vitro* activated with anti-CD3 and anti-CD28 (5 μg/ml) for 24 hours. *In vitro* activated or naïve P14 T cells were resuspended in 20 μl of P3 (P3 Primary Cell 4D-Nucleofector X Kit; Lonza), mixed with sgRNA/Cas9 RNP and electroporated using a Lonza 4D-Nucleofector system (CM137) as previously described.[75] Cells were expanded for 72 hours in the presence of IL-2 (25U/ml; Peprotech). Edited cells were mixed at a 1:1 ratio and 5×10^5 cells were transferred i.v. into LCMV-infected recipients.

Multiome

Single-cell multiome libraries were generated using the 10× Genomics Chromium Next GEM Single-Cell Multiome ATAC + Gene Expression reagent bundle (100285) and the Chromium controller according to the manufacturer's instructions (CG000338-Rev E). GP33-tetramer$^+$ CD8$^+$ T cells were isolated and washed in PBS. Cells were lysed for 3 min (10 mM Tris–HCL, pH 7.4, 10 mM NaCl, 3 mM MgCl2, 0.1% Tween-20, 0.1% NP40, 0.01% digitonin, 1% BSA, 1 mM DTT and 1 U μl−1 RNase inhibitor), washed 3x with 1 ml wash buffer (10 mM Tris–HCL, pH 7.4, 10 mM NaCl, 3 mM MgCl2, 1% BSA, 0.1% Tween-20, 1 mM DTT and 1 U μl−1 RNase inhibitor) before centrifugation at 500*g* for 5 min at 4 °C. The supernatant was discarded, and cells were diluted in 1× diluted nuclei buffer and processed according to the Chromium Next GEM Single-Cell Multiome ATAC + Gene Expression user guide. After transposition and chip loading, cells were loaded into the Chromium Controller instrument to generate single-cell GEMs, followed by incubation in a C1000 Touch Thermal Cycler with 96-Deep Well Reaction Module (Bio-Rad). Barcoded DNA was purified and amplified before ATAC and cDNA library construction. For ATAC, the purified DNA was amplified to enable sample indexing and enrichment of the DNA. cDNA was amplified, purified and quantified using a Bioanalyzer 2100 system (Agilent). The cDNA was subsequently fragmented, PCR-amplified and purified as depicted in the Chromium Next GEM Single-Cell Multiome ATAC + Gene Expression user guide. Fragment files for each sample, containing the unique aligned reads passing filter for each cell barcode, as well as gene expression matrixes, were loaded into ArchR[29] and dimensionality reduction and clustering was performed as previously described (https://greenleaflab.github.io/ArchR_2020/Ex-Analyze-Multiome.html). Gene expression module scores were generated in Seurat using the AddModuleScore() function. Peak signature scores were generated as previously described.[42] Trajectory analysis was performed in ArchR using the addTrajectory() function. Pairwise gene expression analyses were performed in ArchR using the getMarkerFeatures() function.

scATAC-seq

T cell nuclei were isolated and partitioned into gel-bead emulsions that allow barcoded transposition at single-cell scale. The emulsions were broken, the product was cleaned and libraries were prepared for Illumina sequencing according to the 10x Chromium scATAC protocol (https://support.10xgenomics.com/single-cell-atac). Libraries were sequenced on the Illumina HiSeq 4000. Fastq files were trimmed, aligned, and deduplicated using the 10X genomics cellranger-atac count pipeline. Fragment files for each

sample, containing the unique aligned reads passing filter for each cell barcode, were loaded into ArchR.[29] Marker features were identified 'getMarkerFeatures'. GeneScore visualizations were performed using the ArchR implementation of Magic imputation. Motifs enriched in specific peak sets were analyzed using CisBP or JASPAR. For TF expression analysis, previously generated RNA-seq count matrixes were analyzed using DESeq2[72] using the default parameters. T_{RM} samples were compared to their respective T_{CIRC} cell populations using the 'results' function with α=0.05.

QUANTIFICATION AND STATISTICAL ANALYSIS

Statistical analyzes were performed by one- or two-way analysis of variance (ANOVA) test followed by Bonferroni's post-test, Wilcoxon signed-rank test or by two-tailed Student's *t* test using Prism 9 (GraphPad) or R. *P* values were represented by * $p < 0.05$; ** $p < 0.01$; *** $p < 0.001$; **** $p < 0.0001$.